CrossMark

RESEARCH ARTICLE

Experimental analysis of thermo-acoustic instabilities in a generic gas turbine combustor by phase-correlated PIV, chemiluminescence, and laser Raman scattering measurements

Christoph M. Arndt · Michael Severin · Claudiu Dem · Michael Stöhr · Adam M. Steinberg · Wolfgang Meier

Abstract A gas turbine model combustor for partially premixed swirl flames was equipped with an optical combustion chamber and operated with CH_4 and air at atmospheric pressure. The burner consisted of two concentric nozzles for separately controlled air flows and a ring of holes 12 mm upstream of the nozzle exits for fuel injection. The flame described here had a thermal power of 25 kW, a global equivalence ratio of 0.7, and exhibited thermo-acoustic instabilities at a frequency of approximately 400 Hz. The phase-dependent variations in the flame shape and relative heat release rate were determined by OH* chemiluminescence imaging; the flow velocities by stereoscopic particle image velocimetry (PIV); and the major species concentrations, mixture fraction, and temperature by laser Raman scattering. The PIV measurements showed that the flow field performed a "pumping" mode with varying inflow velocities and extent of the inner recirculation zone, triggered by the pressure variations in the combustion chamber. The flow field oscillations were accompanied by variations in the mixture fraction in the inflow region and at the flame root, which in turn were mainly caused by the variations in the CH_4 concentration. The mean phase-dependent changes in the fluxes of CH_4 and N_2 through cross-sectional planes of the combustion chamber at different heights above the nozzle were estimated by combining the PIV and Raman data. The results revealed a periodic variation in the CH_4 flux by more than 150 % in relation to the mean value, due to the combined influence of the oscillating flow velocity, density variations, and CH_4 concentration. Based on the experimental results, the feedback mechanism of the thermo-acoustic pulsations could be identified as a periodic fluctuation of the equivalence ratio and fuel mass flow together with a convective delay for the transport of fuel from the fuel injector to the flame zone. The combustor and the measured data are well suited for the validation of numerical combustion simulations.

Abbreviations

CC	Combustion chamber
IP	Inner plenum
OP	Outer plenum
CL	Chemiluminescence
IRZ	Inner recirculation zone
ORZ	Outer recirculation zone
PIV	Particle image velocimetry
PVC	Precessing vortex core
RMS	Root mean square

List of symbols

D	Diameter
ID	Inner diameter
OD	Outer diameter
f	Frequency
f	Focal length
$f/$	Aperture
l	Length
L	Air mass flow ratio outer/inner nozzle
$\dot{m}$	Mass flow
r, h	Radial, axial position
S	Swirl number
T	Temperature
P_{th}	Thermal power

C. M. Arndt (✉) · M. Severin · C. Dem · M. Stöhr · W. Meier
Institute of Combustion Technology, German Aerospace Center (DLR), Pfaffenwaldring 38-40, 70569 Stuttgart, Germany
e-mail: christoph.arndt@dlr.de

A. M. Steinberg
Institute for Aerospace Studies, University of Toronto, 4925 Dufferin Street, Toronto, ON M3H 5T6, Canada

p	Pressure
u, v, w	Axial, radial, tangential velocity component
X	Mole fraction
Y	Mass fraction

Greek symbols

α	Phase angle
λ	Wavelength
ρ	Density
Φ	Flux
ϕ	Equivalence ratio
ξ	Mixture fraction
τ	Time

Mathematical

$(\bar{\cdot})$	Phase-averaged mean
$(\bar{\bar{\cdot}})$	Time average
$\{\cdot\}$	Property integrated across the field-of-view width (r) at a particular h
$(\cdot)'$	Instantaneous fluctuation
$(\cdot)''$	RMS fluctuation

Index

i	Inner
o	Outer
m	Mass
V	Volume
stoich.	Stoichiometric

1 Introduction

Most gas turbine (GT) combustors for power generation are equipped with swirl burners and operated with lean premixed or partially premixed flames. While such combustors feature excellent emission levels, serious operational restrictions arise from their susceptibility to thermo-acoustic instabilities (Huang and Yang 2009; Lieuwen and Yang 2005), where the unsteady heat release couples with one or more acoustic modes of the combustor. Different feedback mechanisms for thermo-acoustic oscillations have been reviewed in the literature (Candel 2002; Dowling and Stow 2003; Lieuwen and Yang 2005; Lieuwen 2012), such as flame surface density variations (Candel 2002; Schuller et al. 2003), periodic vortex shedding (Schadow and Gutmark 1992), or equivalence ratio fluctuations at the combustor inlet (Lieuwen and Zinn 1998). Equivalence ratio fluctuations can occur in combustors, where fuel is injected close to or inside the swirl generators. Here, pressure fluctuations in the combustion chamber can cause unsteady fuel and air flow rates. If the fuel and air feed systems respond differently to pressure waves generated by unstable combustion, not only the total flow rate fluctuates, but also

the equivalence ratio. Those mixture variations are convected to the flame zone and can cause heat release fluctuations. If the convection time is in resonance with an acoustic eigenmode of the combustor, the fluctuations lead to self-sustained pressure oscillations. This coupling presents a major excitation mechanism in flames with inhomogeneous fuel/air mixtures (Huang and Yang 2009). Further feedback mechanisms include fuel feed line–acoustic coupling and interaction of incident acoustic waves with the swirler (Huang and Yang 2009; Lieuwen and Yang 2005).

Despite significant research effort and progress in this field, reliable prediction of frequencies and amplitudes of thermo-acoustic oscillations remains a challenging task. The main reason for this lies in the complex nature of the interaction between heat release, flow field, and acoustic modes of the combustion system. Frequently, minor geometrical modifications of the combustor or small changes in the operating or boundary conditions lead to drastic changes in the stability of the system, such as transition from attached to detached flames or flames with and without precessing vortex cores (Allison et al. 2012; Arndt et al. 2010; Biagioli et al. 2008; Fritsche et al. 2007; Hermeth et al. 2014; Oberleithner et al. 2015). In addition, understanding and predicting combustor thermo-acoustic behavior is complicated by significant effects of turbulence–chemistry interaction (Bulat et al. 2013; Gicquel et al. 2012; Lückerath et al. 2011; Meier et al. 2006; Rebosio et al. 2010), and spatially and temporally varying degrees of premixing (Bade et al. 2014; Masri 2015; Meier et al. 2007; Stopper et al. 2013). The occurrence of hydrodynamic instabilities like precessing vortex cores, vortex shedding, or other shear layer instabilities (Candel et al. 2014; Caux-Brisebois et al. 2014; Kim et al. 2014; Moeck et al. 2012; Stöhr et al. 2012, 2015; Stöhr and Meier 2013b) further complicates the situation. For example, precessing vortex cores can influence the mixing (Stöhr et al. 2015), or can cause flame role-up and local extinction (Stöhr et al. 2013).

Good progress toward understanding combustion instabilities has been achieved in recent years by the use of GT model combustors. These combustors can feature many phenomena relevant to practical engines, such as self-excited oscillations, swirl-induced vortex breakdown, hydrodynamic instabilities, and time-dependent premixing, while providing well-controlled operating and boundary conditions at reasonable costs. Moreover, they can be designed with good optical access to allow for the application of optical and laser measurement techniques capable of determining important quantities like velocity, temperature, and species concentrations with high spatial and temporal resolution.

For the study of periodic combustion instabilities, phase-correlated measurements, i.e., single-shot or short-exposure

measurements recorded simultaneously with the phase angle of the instability, have been applied to reveal the changes in various quantities during an oscillation cycle. Those measurements include OH* and CH* chemiluminescence to identify heat release variations, OH, CH_2O, and CH PLIF to determine fluctuations in the flame surface density or local Rayleigh index and laser Raman measurements to assess changes in the thermo-chemical state of the flame (Bellows et al. 2007; Biagioli et al. 2008; Giezendanner et al. 2003; Hubschmid et al. 2008; Ishino et al. 2001; Lee and Santavicca 2003; Meier et al. 2007; Schildmacher et al. 2006). More recently, high-speed imaging techniques in combination with acoustic pressure tracing have been applied to study thermo-acoustic instabilities in GT-relevant combustors (Boxx et al. 2010, 2012; Caux-Brisebois et al. 2014; Durox et al. 2013; Galley et al. 2011; Gounder et al. 2014; Steinberg et al. 2010, 2012, 2013; Worth and Dawson 2012), yielding deeper insight into the feedback mechanisms.

In addition to revealing causality of the oscillations, an important role of measurements in GT model combustors is to supply experimental data for simulation validation. Important data include sufficient definition of boundary conditions, along with temperature, major species, and velocity distributions. However, such information often is not provided in GT model combustor studies due to challenges in applying the required diagnostics to complex confined flames. Particularly, the application of laser Raman scattering for single-shot species and temperature measurements in such combustors is demanding, and there are only few data sets available for model validation comprising multispecies concentrations, temperature, and velocity field data. So far, the most comprehensive experimental data sets from GT model combustors are from the DLR Dual Swirl Burner (Giezendanner et al. 2003; Weigand et al. 2006) and the Turbomeca Burner (Meier et al. 2007). They have been operated with gaseous fuels at conditions with and without thermo-acoustic instabilities. In both cases, the instabilities were identified as Helmholtz oscillations at frequencies around 300 Hz. The Turbomeca Burner has been conceived for lean premixed combustion with fuel injected into the air flow within the swirler (Lartigue et al. 2004). In this premixing mode, often referred to as technical premixing, a certain degree of unmixedness is present in the combustion chamber. A comparison with flames that were perfectly premixed far upstream of the combustor revealed that the premixing mode had little effect on the flame shape and chemistry (Dem et al. 2015), but that technically premixed flames were more susceptible to thermo-acoustic instabilities (Im 2012). The DLR Dual Swirl Burner has been designed for partially premixed flames and exhibited some characteristics of aero-engine combustors. The fuel is injected between two co-swirling air flows that are fed from a common plenum through two concentric nozzles. During the transition from thermo-acoustically stable to unstable states, the flame shape changed from conical to flat, i.e., burning close to the burner plate (Stöhr et al. 2013). This behavior was associated with the shape of the outer air nozzle that was contoured with a quarter circle at the exit, so that the air flow was guided radially outward. The contour posed a certain problem for the numerical simulation because the exact location of the detachment of the flow from the quarter circle was difficult to predict correctly (Reichling et al. 2013; See and Ihme 2014, 2015; Widenhorn et al. 2009). Further, the ratio of the mass flows through the two swirlers could not be controlled or measured and thus was a source of uncertainty in the boundary conditions.

Based on this experience, a new generic "standard" burner for gas turbine thermo-acoustics research has been defined within the framework of the German Research Foundation Collaborative Research Center 606. The design is based on the previously studied Dual Swirl Burner configurations, but features several improvements to the boundary conditions. In contrast to the previous combustors, the burner features two swirlers with separate plenum chambers. The air flow to each plenum can be controlled and monitored independently, such that the air split ratio between the inner and outer nozzle can be set exactly. The exit of the outer air flow is a sharp edge instead of a curved profile to achieve a well-defined separation point of the flow. Also, the separation wall between the two air flows was extended to the combustor dump plane in order to achieve better optical access to this region. The burner can be operated either partially or perfectly premixed. The combustion chamber offers very good optical access, and it is equipped with several ports for pressure probes. The combustor described in this paper is operated in the partially premixed mode at atmospheric pressure with gaseous fuel (CH_4). However, a nearly identical setup is available for liquid fuels (Bärow et al. 2013). Further, the design allows for several identical burners to be combined into a combustor array, in order to investigate cross-flame interactions (Kraus and Bockhorn 2013).

The current paper focuses on a detailed experimental characterization of an operating condition where the flame undergoes self-excited thermo-acoustic oscillations. The flame shape was measured by chemiluminescence imaging; the flow field by particle image velocimetry; and the simultaneous major species concentrations, temperature, and mixture fraction by laser Raman scattering. All measurements were taken in combination with dynamic pressure probes in order to off-line-correlate the single-shot measurements with the phase in the thermo-acoustic oscillation. One main goal of this study is the presentation of a novel gas turbine combustor for the analysis of thermo-acoustic instabilities

that is particularly tractable for numerical simulations, along with an extensive experimental data set for simulation validation. Such a configuration/data set fills a significant gap in turbulent combustion test cases (TNF Workshop 2015). Moreover, a detailed analysis is presented for the coupling between the thermo-acoustic oscillations and flow/mixing behavior, with the aim of understanding the underlying feedback mechanism. It includes the phase-dependent variation in the fuel mass flux through axial planes of the combustor and specifies the different contributions to it from fuel mole fraction, axial velocity, and gas temperature. It is shown how the sequence of reactant convective transport, mixing, and reaction events during an oscillation cycle is related to the pressure variation. This feedback mechanism is known as fuel flow rate and equivalence ratio oscillation coupled with a convective time delay, and was previously described in the literature (Candel 2002; Ćosić et al. 2015; Lieuwen and Zinn 1998; Lieuwen and Yang 2005; Meier et al. 2007; Sattelmayer 2003; Schürmans et al. 2004). This analysis establishes a quantitative means of evaluating coupling mechanism predicted by simulations. The results of this study will be used as basis for numerical simulations as well as for further, detailed experimental studies of different phenomena in this combustor.

2 Experimental

2.1 Combustor

A schematic of the combustor is shown in Fig. 1. It consists of an inner nozzle (diameter $D = 15$ mm) and a concentric annular nozzle (ID = 15.2 mm, OD = 24 mm), which are fed with air at room temperature from two separate plenums. Both flows are swirled in the same direction by separate radial swirl generators. The separate air supplies allow controlled adjustment of the air split ratio, $L = \dot{m}_{air,o}/\dot{m}_{air,i}$, where $\dot{m}_{air,o}$ and $\dot{m}_{air,i}$ are the air mass flow rates through the outer and inner nozzles, respectively. The theoretical swirl number is $S_o = 1.06$ for the outer swirler and $S_i = 0.73$ for the inner swirler. Fuel is supplied to the inner nozzle through a feed system built into the splitter wall between the nozzles. The fuel flows through a circle of 60 holes with diameter of 0.5 mm located on the inner wall surface 12 mm below the nozzle exit. In this configuration, the flow from the inner nozzle is partially premixed before the onset of combustion. Alternatively, or in addition, fuel can be supplied far upstream of the air plenums in order to operate premixed flames or partially premixed flames with various degrees of premixing. However, these latter configurations are not studied here.

The flames are enclosed in a square combustion chamber (CC) (89×89 mm² cross section, 112 mm high)
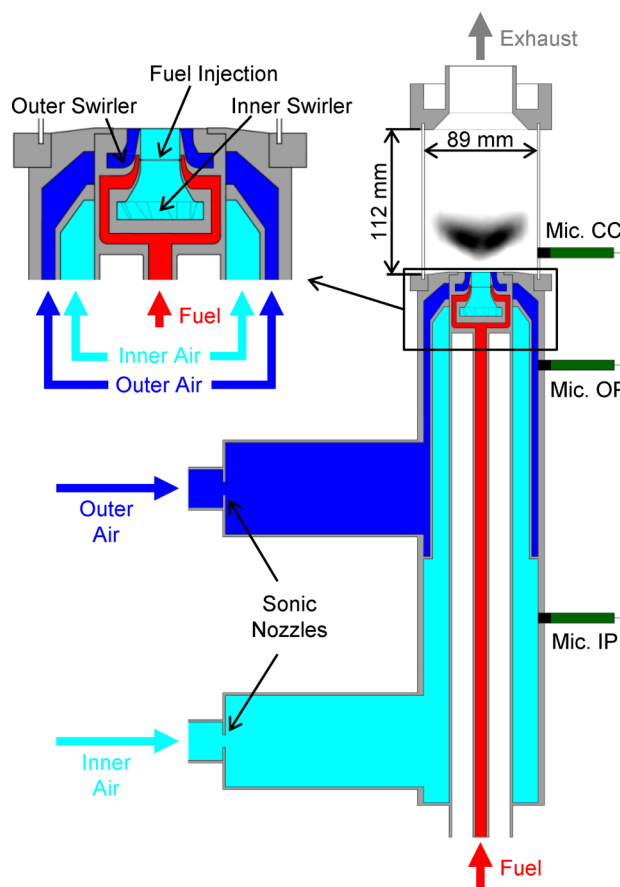
Fig. 1 Schematic drawing of the burner with combustion chamber and the air and fuel supplies. *Mic.* means microphone, *CC* combustion chamber, *OP* outer plenum, and *IP* inner plenum

comprised of four fused silica plates held by steel frames. The frames are mounted to four posts in the corners and to the bottom and top of the combustion chamber. The unrestricted view of the flame is 73 mm wide and 112 mm high on each side. The burner face plate has a slight conical shape, such that the nozzle exit is elevated by 2 mm with respect to the outer edge of the face plate. This enables better optical access to the nozzle exit. The coordinate system origin for all measurements is the center of the nozzle exit ($h = 0$, $r = 0$). The exit of the vertically oriented combustion chamber was conically shaped, leading to a short central exhaust pipe with an inner diameter of 50 mm. Two of the four posts are each equipped with three ports for the installation of microphone probes.

The lower part of the combustor, containing the air plenums and supply lines, also is shown in Fig. 1. The outer housing is machined from a square cross-sectional stainless steel tube with inner dimensions of 90×90 mm². Air is supplied to the plenums from two tubes (ID = 72 mm) on one side. To yield defined upstream acoustic boundaries, sonic orifices are located approximately 200 mm upstream

of the inlet to the vertical plenum sections. The inner air plenum (IP) extends over the complete length (380 mm) of the feed system. A round tube (OD = 50 mm) along the burner axis forms the inner boundary of the inner plenum. In the upper half of the burner, the outer boundary of the inner plenum is a 76 mm ID tube that separates the inner and outer plenum. In the lower half of the burner, the outer boundary of the inner plenum has a 90×90 mm^2 square cross section formed by the overall burner geometry. The vertical section of the outer air plenum (OP) has a length of 200 mm, a round inner surface with a diameter of 80 mm, and an outer boundary of 90×90 mm^2. Fuel is fed through a 4 mm ID tube along the burner axis to a small fuel plenum at the nozzle. Ports for microphone probes enable the registration of acoustic oscillations in the plenums. Their locations are indicated in Fig. 1.

All flow rates were metered by electromechanical mass flow controllers (Brooks type 5851S for CH$_4$ and type 5853S for each air flow) and additionally monitored by calibration-standard Coriolis flow meters (Siemens SITRANS F C MASS 2100 DI 3 for CH$_4$ and Siemens SITRANS F C MASS 2100 DI 15 for each air flow) with an accuracy of approximately 1.5 %.

For the results presented in this paper, the burner was operated in the partially premixed configuration with $\dot{m}_{air,o} = 451$ and $\dot{m}_{air,i} = 282$ g/min of air in the outer and inner plenum, respectively, and $\dot{m}_{CH_4} = 30$ g/min of CH$_4$. The corresponding thermal power was $P_{th} = 25$ kW, the global equivalence ratio was $\phi_{global} = 0.7$, and the global stoichiometric mixture fraction was $\xi_{global} = 0.0391$. The mass flow ratio of $L = 1.6$ between outer and inner air is approximately the ratio of the nozzle exit areas, resulting in similar bulk velocities and equal pressure drop across both swirlers. With these flow rates, but without a flame in the combustion chamber, the pressure drop was $\Delta p_{air} = 14$ mbar (1.5 %) across the air swirlers and $\Delta p_{fuel} = 70$ mbar (7.3 %) across the fuel injector.

2.2 Pressure measurements

The pressure oscillations in the combustion chamber and in the two air plenums were measured using calibrated microphone probes (Brüel & Kjær, type 4939), with a sampling rate of 50 kHz. The microphone probes were calibrated for frequencies up to 2000 Hz; higher frequencies are not studied here. The pressure signal in the combustion chamber was used as the reference signal for off-line phase-conditioning of the laser-based measurements as described below.

The pressure power spectrum at each location was computed by slicing the long-duration pressure signal into one-second segments, calculating the spectrum for each segment, and then averaging the results from each segment.

No additional filtering or smoothing of the raw signals or the frequency spectra was performed.

As will be seen below, the dominant thermo-acoustic frequency was $f = 392$ Hz. Off-line phase correlation of the laser measurements (described below) therefore was performed to study the thermo-acoustically coupled flow and flame behavior. Pressure and single-shot laser measurements were recorded simultaneously, and each single-shot laser measurement was correlated with a combustion chamber pressure. In post-processing, the measured values were sorted with respect to the phase angle (α) through the oscillation and, for phase-correlated mean values, averaged within eight bins each comprising 45° phase angle span. Phase angle 0° was defined as the transition from negative to positive pressure fluctuation in the combustion chamber. Accordingly, phase 1 covered the range between $-22.5° < \alpha < +22.5°$ (termed ph1), phase 2 the range between $22.5° < \alpha < 67.5°$ (ph2), etc.

At the temperatures prevailing in the combustion chamber ($T \approx 1800$ K), a frequency of 392 Hz corresponds to a wavelength of $\lambda \approx 2$ m. Thus, spatial pressure gradients within the combustion chamber were small and are neglected in the following treatment.

2.3 Flow field measurements

Three-component velocity fields were measured using stereoscopic particle image velocimetry (PIV) at a repetition rate of 5 Hz. The system (FlowMaster, LaVision) consisted of a frequency-doubled dual-head Nd:YAG laser (New-Wave Solo 120), two CCD cameras (LaVision Imager Intense, 1376×1040 pixels), operated in double-frame mode, and a programmable timing unit (PTU 9, LaVision). The laser pulse energy was 120 mJ at 532 nm, and the separation time between two pulses was 11 µs. The laser beam was expanded into a light sheet that covered the central vertical plane of the combustion chamber. The thickness of the laser sheet was around 1 mm. The cameras were equipped with a wide-angle lens ($f = 16$ mm, set to f/2) and a band-pass filter (532 ± 5 nm) in order to reduce the influence of flame luminosity. Both cameras were mounted on Scheimpflug adapters in order to align their focal plane with the laser sheet. Both fields of view covered an area -39 mm $< r < 39$ mm and 0.5 mm $< h < 105$ mm. The distance between the camera lenses and the measurement plane was 200 mm, and the viewing angle of each camera with respect to the normal of the laser sheet was 20°. An infrared filter was mounted between the combustor and the cameras in order to protect the cameras from thermal radiation.

The air flow was seeded with TiO$_2$ particles with a nominal diameter of 1 µm, which have a relaxation time of $\tau \approx 5 \times 10^{-6}$ s. For the condition tested, the strongest local

velocity differences of $\Delta v \approx 40$ m/s occur over a length scale of $l \approx 10$ mm. The resulting Stokes number is ($\tau \Delta v)/l = 0.02$, and thus, velocity errors due to particle slip are considered negligible. 1200 single-shot particle pairs were recorded, and velocity fields were evaluated from these particle image pairs using a commercial PIV software (LaVision Davis 8.0). A multiscale cross-correlation algorithm was used with a final interrogation window size of 16×16 pixel, corresponding to an in-plane spatial resolution of 1.5×1.5 mm^2, and a window overlap of 50 %. Based on the ± 0.1 pixel uncertainty of the peak-finding algorithm, the maximum random uncertainty of in-plane instantaneous velocities is ± 0.8 m/s. With the camera angle of $20°$, the uncertainty of the out-of-plane velocity is about three times higher than in-plane uncertainty (Lawson and Wu 1997).

2.4 Laser Raman measurements

Single-shot laser Raman scattering was applied for the pointwise quantitative measurement of the major species concentrations (O_2, N_2, CH_4, H_2, CO, CO_2, H_2O) and the temperature. The measurement system has been described previously (Keck et al. 2002; Meier et al. 2007), and only a short summary is given here. The radiation of a flashlamp-pumped dye laser (Candela LFDL 20, wavelength 489 nm, pulse energy ≈ 1.8 J, pulse duration ≈ 3 μs, pulse repetition rate 5 Hz) was focused into the combustion chamber, and the Raman scattering emitted from the measurement volume (length ≈ 0.6 mm, diameter ≈ 0.6 mm) was collected by an achromatic lens ($D = 80$ mm, $f = 160$ mm) and relayed to the entrance slit of a spectrograph (SPEX 1802, $f = 1$ m, slit width 2 mm, dispersion ≈ 0.5 nm/mm). The dispersed and spatially separated signals from the different species were detected by individual photomultiplier tubes (PMTs) in the focal plane of the spectrograph and sampled using boxcar integrators. The species number densities were calculated from these signals using calibration measurements, and the temperature was deduced from the total number density via the ideal gas law. The simultaneous detection of all major species with each laser pulse also enabled the determination of the instantaneous mixture fraction (Bergmann et al. 1998). The mixture fraction is calculated following the method by Bilger et al. (1990) and is defined as the ratio of the mass in a sample originating from the fuel stream (here: all C and H atoms) to the total mass.

Raman measurements were taken at a total of 70 measurement locations at heights $h = 8, 15, 20, 25, 40, 50, 60, 70$, and 80 mm above the burner nozzle at various radial locations between $r = -3$ and 27 mm. Measurement locations with $h < 8$ mm and $r > 27$ mm were not accessible due to clipping of the solid angle of the detection optics. For 38 locations at heights from 8 to 40 mm, measurements

were taken with simultaneous pressure recordings to allow for off-line phase correlation with the pressure signal. Further downstream ($h \geq 50$ mm), phase-dependent variations in the thermo-chemical state in the measurement region were insignificant. For $h = 8, 20, 25$, and 40 mm, 2,500 single-shot measurements were taken at each radial location; approximately 1750 measurements were taken at each value of r for $h = 15$ mm. This resulted in approximately 310 measurements (only 220 at $h = 15$ mm) in each of the phase-angle ranges used for conditional averaging. At the locations without conditional averaging, 400 single-shot measurements were obtained. Figure 12a shows the locations of the Raman measurements, with closed symbols indicating the locations of the phase-resolved measurements and open symbols indicating non-phase-resolved locations.

With respect to measurement uncertainties, it must be distinguished between systematic errors arising from, for example, uncertainties in the calibration procedure, and statistical errors which are mainly caused by the statistics (shot noise) of the detected Raman photons (NP) in a single-shot measurement. Systematic uncertainties were typically ± 3–4 % for the temperature and mixture fraction, and ± 3–5 % for the mole fractions of O_2, H_2O, CO_2, and CH_4. Because of the low concentrations of H_2 and CO in the flames investigated, the uncertainty is relatively large for these species. These are estimated to be around ± 20 % at a mole fraction of 0.01. The statistical uncertainties were approximately 30 % larger than stated in a previous study (Meier et al. 2007) due to a lower pulse energy applied in the current measurements. Typical statistical uncertainties (for a single-shot measurement) were 3–3.5 % for the temperature and mixture fraction, 4 % for H_2O, and 9 % for O_2 and CO_2 in the exhaust gas. More details are given in references (Duan et al. 2005; Meier et al. 2007).

2.5 Chemiluminescence measurements

OH* chemiluminescence (CL) was recorded with an intensified high-speed CMOS camera (LaVision HSS 5 with LaVision HS-IRO, active array 512×512 pixels), equipped with a fast UV lens ($f = 45$ mm, f/1.8, Cerco) and a high-transmission band-pass filter (transmission >80 % at 310 nm). The recorded images had a field of view of -39 mm $< r < 39$ mm and 0 mm $< h < 75$ mm. 8200 individual images were recorded at a frame rate of 10 kHz with an exposure time of 15 μs. After darkfield and whitefield corrections, the largest remaining error was due to reflections of OH* chemiluminescence radiation at the combustion chamber walls and bottom, and thermal radiation from the combustion chamber.

OH* chemiluminescence intensities from lean premixed flames are regarded as an indicator for the heat release rate

(Haber and Vandsburger 2003; Hardalupas et al. 2010), but the correlation between OH* chemiluminescence and heat release rate may be influenced by several effects, e.g., turbulence level (Ayoola et al. 2006) or signal trapping (Brockhinke et al. 2012; Sadanandan et al. 2012). Thus, in the current study, only qualitative information is derived from the chemiluminescence images, such as phase-dependent variations in heat release and the location and extension of the flame zone. Although this technique yields line-of-sight integrated signals, spatially resolved information can be gained by deconvolution, taking advantage of the statistical rotational symmetry of the flame. This results in a "quasi 2D image" of the center plane, where the local distribution of the chemiluminescence can be identified more clearly than in the integral view. It is noted that the deconvoluted images inherently average over any periodic asymmetries in the flame associated with, e.g., precessing vortex cores, and therefore do not capture these effects. Nevertheless, they are very insightful for elucidating thermo-acoustically coupled convective processes.

2.6 Numerical modelling of the acoustic eigenmodes of the combustor

Detailed acoustic characterization of the combustor geometry was performed using the Comsol software package (Reuer 2013). A 3D finite-element model solving the acoustic Helmholtz equation was applied. The geometry included the entire combustor except the fuel supply and was discretized with a mesh of 930,000 tetrahedrons. The upstream end of the model domain is a sound hard boundary at the position of the sonic orifices at the plenum inlet. At the downstream exit of the combustion chamber, a perfectly matched layer was attached, which absorbs pressure waves independent of their frequency or incident angle. This provides an easy way to model an open end without the need to simulate a large domain outside the combustor. In the combustion chamber, the spatial distribution of density and sound velocity was modeled based on the Raman measurements. For the excitation of the acoustic modes, a flow point source was included in the model at the position of the flame. The numerical model allowed the determination of the acoustic eigenmodes of the system, such that an assignment of measured frequencies to geometric modes of the combustor was possible.

3 Results and discussion

3.1 General flame behavior and acoustics

In addition to the primary test case described in Sect. 2.1, which was studied in detail, the basic combustor
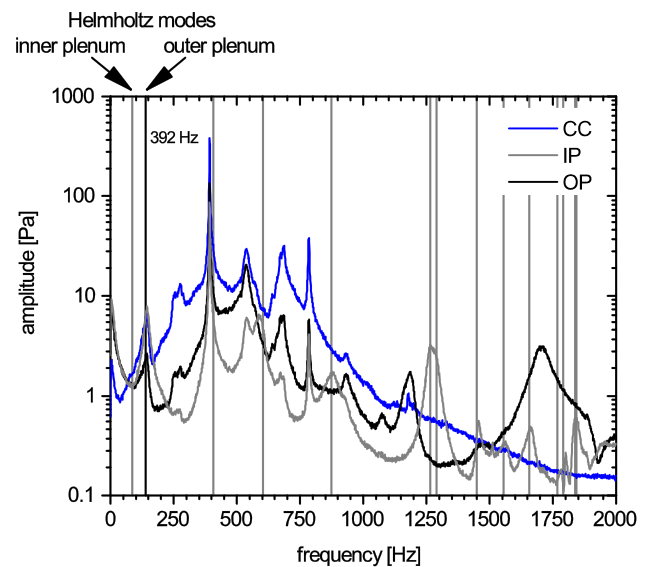
Fig. 2 Acoustic spectra of the standard case measured in the combustion chamber (CC), the outer plenum (OP), and inner plenum (IP). The vertical lines are the computed eigenmodes of the inner plenum (*gray vertical lines*) and the Helmholtz mode of the outer plenum with the combustion chamber (*black vertical line*)

behavior was tested over the range $P_{th} = 10$ kW to 35 kW and $\phi_{global} = 0.55$ to 0.94 (Severin 2012). For $\phi_{global} < 0.65$, the flame was near blow off, and the heat release was distributed across a large axial distance in the combustor. For $\phi_{global} \geq 0.65$, the flame had a V-shape that is typical for many swirl-stabilized flames. The V-shape of the flame did not fundamentally change with either ϕ_{global} or P_{th}, but did increase in overall size and intensity with thermal power. Transition from a V-shape to an M-shape, often associated with a step-change increase in thermo-acoustic amplitude (Arndt et al. 2010; Renaud et al. 2015), was not observed at any tested condition. Instead, the sound pressure level increased essentially linearly from $p''_{CC} = 140$ Pa (137 dB, RMS of the combustion chamber pressure) at $P_{th} = 15$ kW and $\phi_{global} = 0.7$ to $p''_{CC} = 400$ Pa (146 dB) at $P_{th} = 35$ kW and $\phi_{global} = 0.9$.

Detailed analysis of the flame thermo-acoustic behavior was performed using the laser and optical measurements for the case described in Sect. 2.1 ($P_{th} = 25$ kW, $\phi_{global} = 0.7$, $\xi_{global} = 0.0391$). The pressure spectra for this case, recorded in the combustion chamber and the two air plenums (OP and IP), are shown in Fig. 2. The dominant peak for all measurement locations is at 392 Hz. The frequency spectrum from the combustion chamber further exhibits a sharp peak at 785 Hz, corresponding to the second harmonic and broader peaks around 535 and 684 Hz.

As can be seen in Fig. 2, the frequency spectra of the air plenums contain multiple peaks, which were found to correspond to resonances with length scales of the combustor.

For better comparison, the computed eigenmodes of the inner plenum are shown in Fig. 2 as gray vertical lines. The Helmholtz mode between the combustion chamber and the inner plenum, which was found to be the dominant thermo-acoustic mode in previously described setups (Giezendanner et al. 2003; Meier et al. 2007; Weigand et al. 2006), was found to be at 86 Hz. The Helmholtz mode of the combustion chamber with the outer plenum (139 Hz, black vertical line) also is shown in Fig. 2. Neither Helmholtz mode generated dominant acoustic modes in the measured frequency spectra; no peak is visible for the inner plenum Helmholtz mode and only a minor peak for the outer plenum Helmholtz mode. In the present setup, the dominant thermo-acoustic mode was at 392 Hz, which is a resonance mode with $\lambda = 2\, l_{IP}$ (based on the speed of sound in cold air), where l_{IP} is the length of the inner plenum (380 mm). The computed corresponding eigenmode was at 407 Hz. The difference in frequency can be explained by slight temperature and thus speed of sound differences between the simulation and the actual experiment. Figure 3 shows the computed pressure phases for this mode. In the lower part of the inner plenum, a node can be seen (interface between the orange- and blue-colored sections of the inner plenum); the upper and the lower half of the plenum are out of phase, thus resembling a half wave of the inner plenum.

The 392-Hz mode and its harmonic were also identified in the spectral analysis of OH* chemiluminescence signals (measured at 10 kHz repetition rate) and can thus be categorized as thermo-acoustic oscillations. It therefore can be concluded that the dominant mode at 392 Hz corresponds to a thermo-acoustic instability triggered by the interaction between the flame and the inner plenum.

Figure 4 shows the pressure fluctuations $(p' - \bar{\bar{p}})$ recorded in the combustion chamber and the plenum chambers, as well as the fluctuation of the 10 kHz OH* chemiluminescence signal $\left(\left(OH^{*\prime} - \overline{OH^*} \right) / \overline{OH^*} \right)$, that demonstrate this mode. The highest RMS pressure oscillation ($p''_{CC} = 287$ Pa) occurred in the combustion chamber. The corresponding values from the inner and outer plenums were $p''_{IP} = 69$ Pa and $p''_{OP} = 93$ Pa, respectively. While the pressure from the outer plenum followed the pressure variation in the combustion chamber quite closely, the pressure in the inner plenum lagged the pressure in the combustion chamber by an average value of approximately 120°.

3.2 Flame shape oscillations

The flame shape and its periodic variation were visualized by OH* CL imaging. The instantaneous CL images were recorded simultaneously with the pressure in the combustion chamber and sorted with respect to the acoustic phase as described in Sect. 2.1. Figure 5 shows the phase-correlated mean (Fig. 5a) and deconvoluted (Fig. 5b) values of


Perfectly Matched Layer (PML)
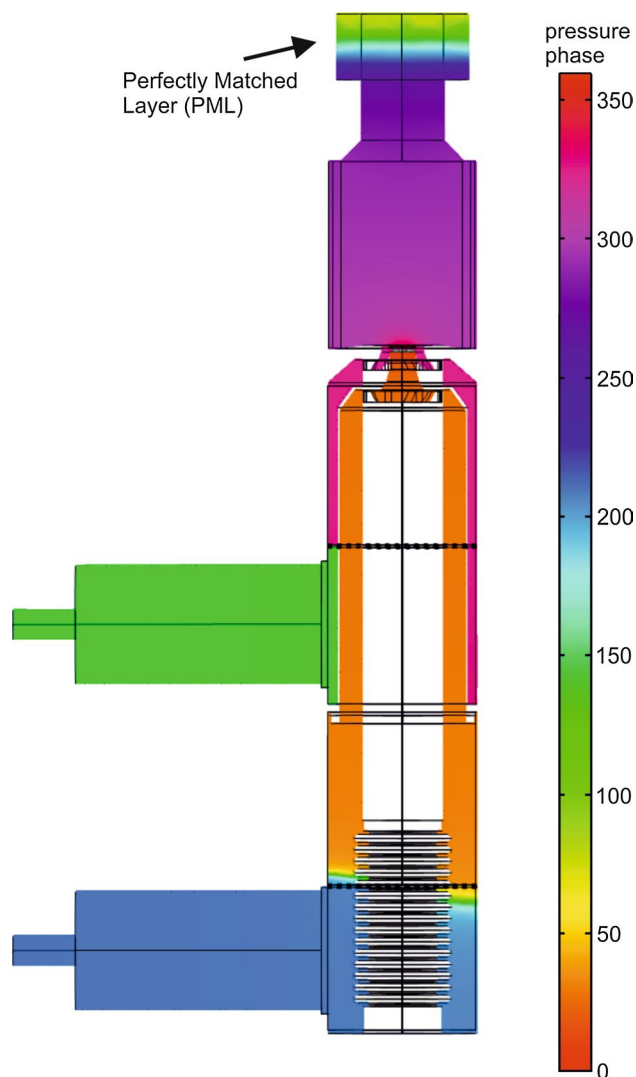
pressure phase

Fig. 3 Computed pressure phases of the 407-Hz eigenmode of the inner plenum

the OH* CL distribution for the eight phase-angle ranges used. In the deconvoluted CL distributions, the high intensities seen at the combustor walls mostly stem from the combustion chamber posts and reflections at the windows. These features are exaggerated by the deconvolution procedure. The spots of increased intensity on the center axis also are artefacts of the deconvolution.

The distributions demonstrate the conical shape of the mean flame zone. The flame was lifted from the nozzle by approximately 8 mm, with the lift-off height moving slightly in axial direction over an acoustic cycle. However, the change in lift-off height is very small in comparison with other studies (Biagioli et al. 2008). The apex angle of the flame zone was roughly 90° with small phase-dependent variations. The flame zone extended to $h \approx 50$–60 mm and covered the whole width of the combustion chamber.
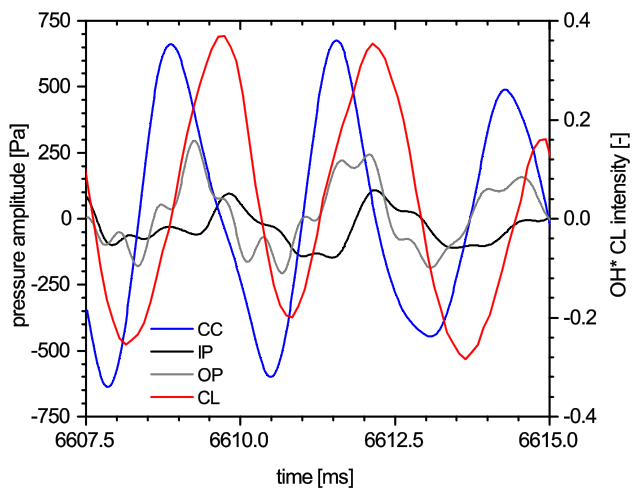
Fig. 4 Example of an extract from the pressure traces measured in the combustion chamber (CC), the outer plenum (OP), and inner plenum (IP) together with the chemiluminescence signal

The size and intensity of the mean chemiluminescence varied during an oscillation cycle, with the maximum and minimum occurring at ph4 and ph8, respectively. According to the definition of α, the maximum and minimum pressures in the combustion chamber were at ph3 ($\alpha = 90°$) and ph7 ($\alpha = 270°$). Thus, pressure and heat release oscillations were out of phase by approximately 45°, but still in the range of positive acoustic energy transfer according to the Rayleigh criterion (Poinsot and Veynante 2012).

Figure 6 shows a summation of the chemiluminescence intensity over horizontal pixel lines for each downstream location and phase angle based on the distributions shown in Fig. 5a. This yielded the chemiluminescence integrated over cross-sectional planes as a function of h. The maximum intensity was found at an average of $h = 35$ mm with a phase-dependent variation of ± 2.5 mm. The axial movement of the mean flame zone was thus quite small. As was seen in Fig. 5a, the maximum heat release is reached in ph4 at $h = 36$ mm.

3.3 Flow field oscillations

Figure 7 shows two-dimensional distributions of the mean (averaged over all phases) axial and radial velocity. The arrows indicate the streamlines and the colors the magnitude of the axial ($\bar{\bar{u}}$, top frame) and radial ($\bar{\bar{v}}$, bottom frame) velocity components; the tangential component ($\bar{\bar{w}}$) is not depicted in these images. The white lines indicate the boundaries of the recirculation zones, i.e., zero mean axial velocity. The mean flow field is typical for swirl flames, exhibiting a conical inflow region with high velocities, a pronounced inner recirculation zone (IRZ), outer recirculation zones (ORZ), and the corresponding shear layers.

It must be kept in mind that the averaged flow fields are significantly different from the instantaneous velocity distributions. To illustrate this, Fig. 8 displays an example distribution from a single-shot PIV measurement. It is seen that the instantaneous flow field is dominated by turbulent structures. The IRZ, for example, does not resemble a large toroidal vortex as in the mean distribution, but is comprised of several smaller unsteady vortices and flow structures. These add up to a large recirculation bubble in the average flow field. The zigzag pattern of vortices in the inner shear layer is a two-dimensional cut through the 3D structure of a helical precessing vortex core (PVC), which is often observed in swirl-stabilized flames (Galley et al. 2011; Moeck et al. 2012; Steinberg et al. 2013; Stöhr et al. 2012; Terhaar et al. 2015). The signature of the PVC can be seen in the frequency spectrum of the pressure in the combustion chamber and the outer plenum (Fig. 2), at a precession frequency of $f_{\text{PVC}} = 1177$ Hz. The presence of the PVC was further confirmed by proper orthogonal decomposition of the velocity fields, according to the method by Stöhr et al. (2012) (not shown here). The analysis of the thermo-acoustic oscillation presented here averages over the motion of the PVC, and therefore, the zigzag vortex pattern does not appear in the phase-averaged flow fields.

Because unsteady vortices and turbulence obscure the phase-dependent changes in the flow field, phase-correlated mean values are considered to reveal the effects of the thermo-acoustic oscillation. During an oscillation cycle, the most prominent variations were observed for the radial velocity component. An overview of these variations is given in Fig. 9, where 2D distributions of the phase-correlated mean values are displayed for four phases (ph1, ph3, ph5, ph7). Approximately 150 single-shot images have been averaged for each phase. The white line again represents the boundary of the recirculation zones (zero axial velocity). It is seen that the IRZ varied significantly in size, with a maximum extent around ph1 and a minimum extent around ph5. The inflowing jet undulated, and the magnitude of the radial velocity was well correlated with this undulation, like a wave that traverses through the lower half of the combustion chamber. Corresponding movements are also seen in the ORZ.

Details of the flow field behavior are better seen in the radial profiles of the phase-correlated mean velocities ($\bar{u}, \bar{v}, \bar{w}$). The heights $h = 8$ and 15 mm, shown in Fig. 10, match axial positions at which Raman measurements have been taken. At these heights, the flows from the two nozzles had largely merged. Only the tangential velocity at $h = 8$ mm still exhibited a clear influence of the two air flows. The IRZ was well pronounced, with a maximum backflow velocity on the axis of $\bar{u} \approx -26$ m/s around ph3 and ph4.

The radial extents of the inflowing jet and the IRZ changed considerably during an oscillation cycle, driven

(a)

(b)
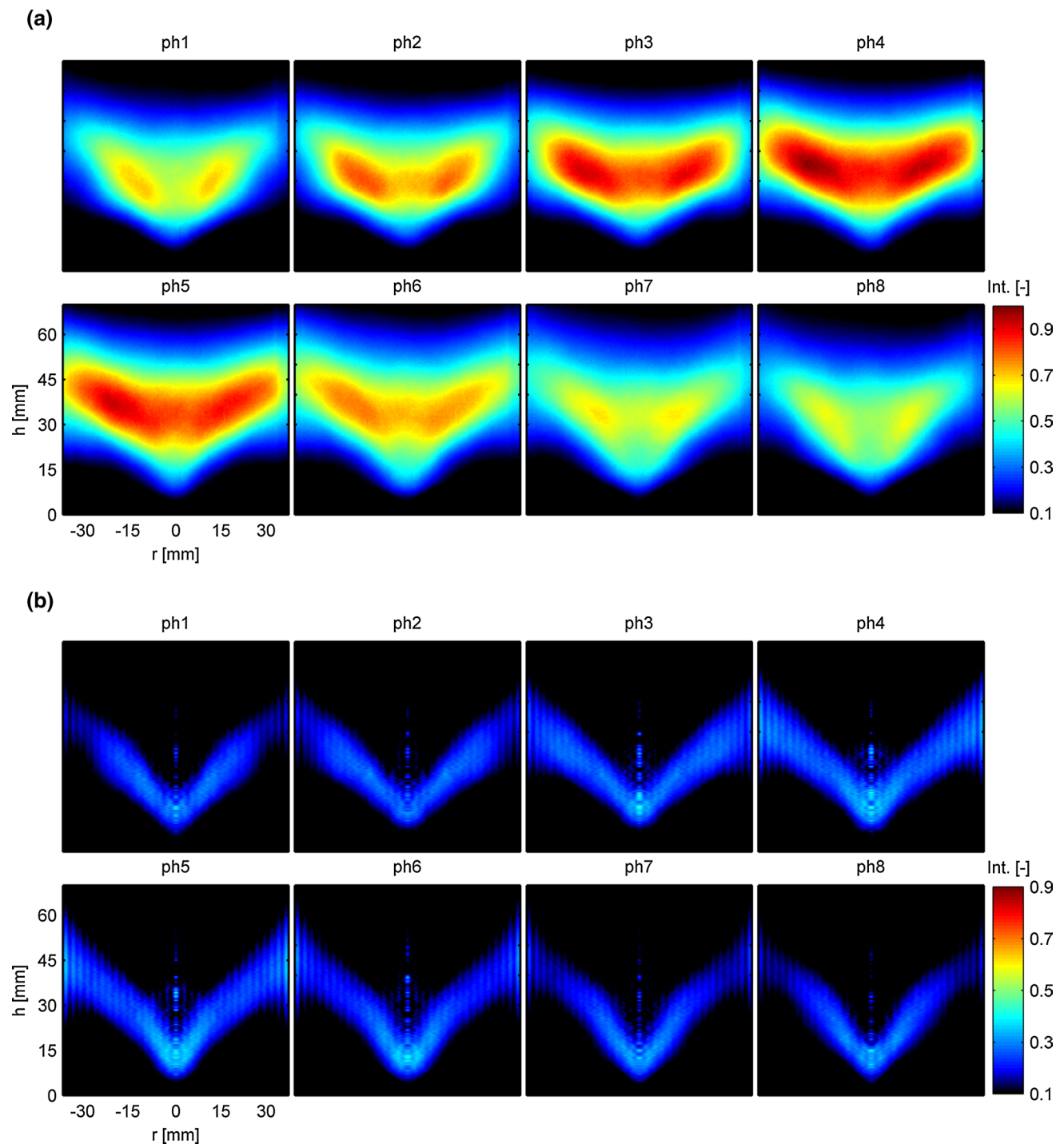
Fig. 5 Phase-correlated mean (**a**) and deconvoluted mean (**b**) OH* chemiluminescence distributions

by the phase-dependent pressure changes at the nozzle. The radial velocity component exhibited the strongest phase-dependent variations, however, not in phase with the axial velocity (out of phase by roughly 90°). The phase angle at which the maximum and minimum velocities were reached changed with increasing height. This reflects the wave-like

motion in the combustion chamber that was previously seen in Fig. 9. A closer analysis of this "pumping mode" will be given after the presentation of the species and temperature profiles.

Figure 9 showed that the shape of the IRZ varied only slightly in the lower part of the combustor ($h < 20$ mm)
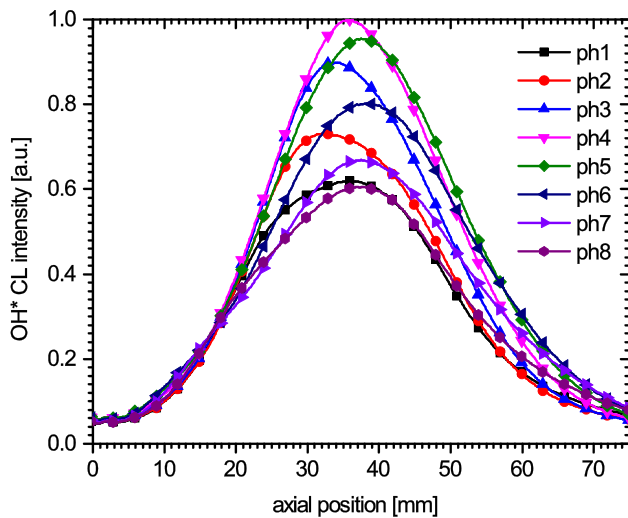
Fig. 6 Phase-correlated axial intensity profiles of the OH* chemi-luminescence distribution. For better discrimination between the curves, symbols are only plotted for each 20th measurement point

during an oscillation cycle, but changed significantly within (20 mm < h < 50 mm) and above (h > 50 mm) the main heat release zone. It is plausible that these phase-dependent variations are related to the thermal expansion within the flame zone and the corresponding decrease in swirl number, because the establishment of an IRZ is connected to the swirl number (Gupta et al. 1984; Lilley 1977). The swirl number is defined as the ratio of the axial flux of angular momentum to the axial flux of axial momentum (Syred and Beér 1974). With increasing axial position, the variations in tangential velocity with phase number decreased; for $h \geq 40$ mm, no clear phase dependency was observed (not shown). However, the axial velocity component behaved differently. Figure 11 displays radial profiles of the phase-correlated mean axial velocity at $h = 25$, 40, and 50 mm. For clarity, results from only four phases are shown. Up to $h \approx 40$ mm, the phase-dependent variations in the maxima of the profiles decrease with increasing downstream position; this trend however is reversed at $h = 50$ mm, where a significant variation in the maxima of the profiles can be observed. Here, the profile at ph4 exhibits the highest mean axial velocity, whereas the profile at ph8 exhibits the lowest mean axial velocity. This reflects the phase-dependent variation in the heat release, as shown in Figs. 5 and 6. Thus, the variation in the thermal expansion at $h \geq 40$ mm leads to a change in axial momentum and swirl number, as expected. At phases with low axial velocity, the swirl number is high, and consequently, the IRZ is rather large and exhibits maximum backflow velocities. The changes in size of the IRZ are thus directly coupled to the changes in heat release. Similar observations of swirl number waves have previously been made in thermo-acoustically oscillating
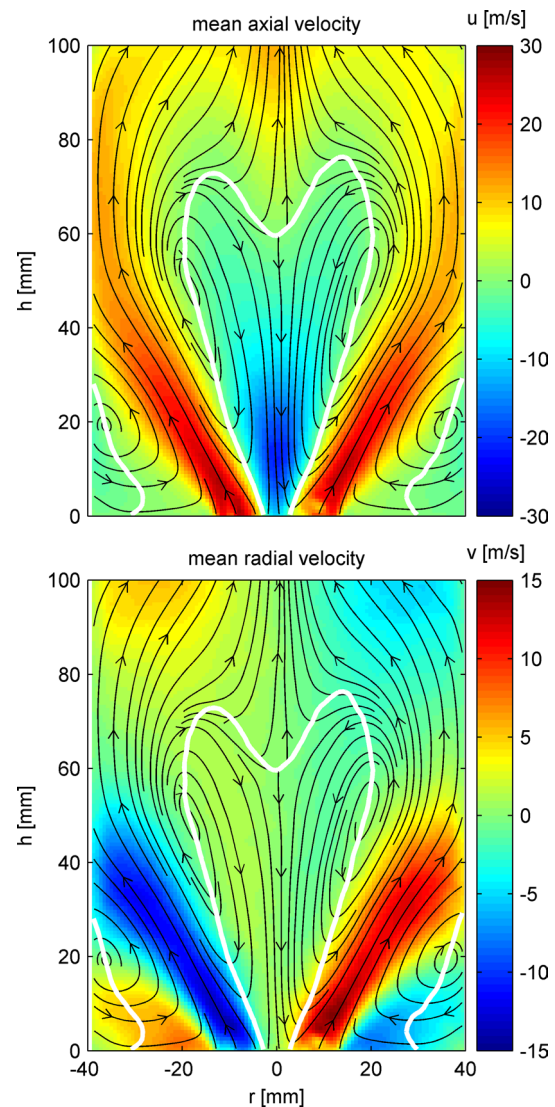
Fig. 7 Velocity distributions averaged over all phases. Streamlines indicate flow direction. *Top frame*: Color-coded mean axial velocity. *Bottom frame*: Color-coded mean radial velocity

swirl flames (Caux-Brisebois et al. 2014; Komarek and Polifke 2010; Palies et al. 2010, 2011).

3.4 Variations in mixture fraction and temperature

Because the flow from the central nozzle was partially premixed and the flow from the annular nozzle was pure air, significant spatial and temporal variations in mixture fraction are expected purely due to turbulence. Furthermore, the thermo-acoustic oscillations are expected to cause cyclical variations in the mixture fraction statistics, as was seen in previous studies (Ćosić et al. 2015; Franzelli et al. 2012; Lieuwen and Zinn 1998; Meier et al. 2007; Sattelmayer 2003). To present an overview of the

phase-correlated Reynolds-averaged values of the mixture fraction distribution, the results from the point measurements were interpolated to yield two-dimensional plots using the software "Origin 9.1." Because the grid pattern of measurement locations was relatively coarse, with only 38 locations of phase-correlated measurements, the spatial structures are not finely resolved. However, the 2D images yield a good overview.

In Fig. 12a, the results are displayed for the area $r = 0$–27 mm and $h = 8$–60 mm. At $h = 8$ mm, the values of the phase-conditioned Reynolds-averaged mixture fractions, $\bar{\xi}$, across all radial locations and phase angles, spanned a range from $\bar{\xi} = 0.0126$–0.0838, which
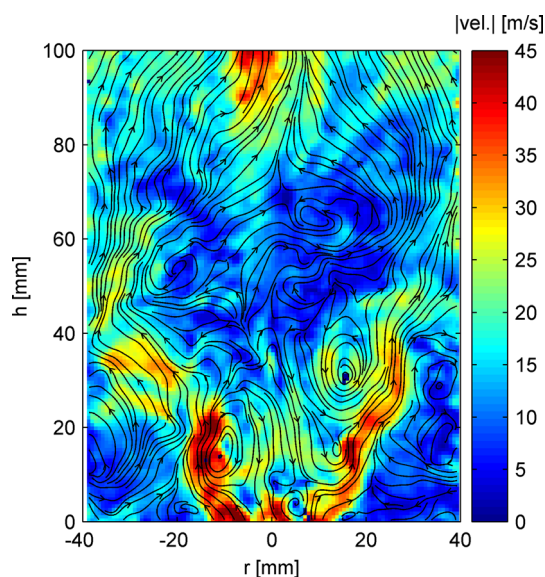
corresponds to equivalence ratios of $\bar{\phi} = 0.22$–1.57, respectively. The variations were rapidly mixed, so that at $h = 40$ mm, $\bar{\xi}$ varied only between 0.041 and 0.044 across the radius. At $h = 80$ mm, the mixture fraction averaged over all phase angles and radial locations was $\bar{\bar{\xi}} = 0.0420$, which is larger than the mixture fraction deduced from the flow rates ($\xi_{global} = 0.0391$). Since the 2D mixture fraction plots indicate lower values of $\bar{\xi}$ with increasing r, this deviation is probably caused by richer mixtures in the Raman measurement area ($r \leq 27$ mm) than in the area from $r = 27$ to 44.5 mm. The mixture fraction distributions clearly evidence cyclic variations, with richer mixtures entering the combustion chamber around ph1. During the following phase angles, the regions of richer mixtures expand downstream while being diluted by turbulent mixing.

The variations in mixture fraction are largely correlated with those of the CH_4 distribution, shown in Fig. 12b, at least up to $h \approx 20$ mm. The distributions reflect the penetration depth of the fuel, and yield an impression of its dilution and consumption. The highest mean CH_4 mole fraction was $\overline{X}_{CH_4} = 0.127$ and occurred at $h = 8$ mm. The decrease in $\overline{X}_{CH_4}$ with downstream distance correlates well with the shape of the flame zone measured by OH* CL (see Fig. 5), in the sense that the regions of decreasing fuel mole fractions coincide with the regions of chemiluminescence.

Figure 12c shows the corresponding temperature distributions. The temperature of the inflowing jet gradually increased with height and reaction progress. The highest mean temperatures occurred in the IRZ at $h \approx 20$ mm. Phase-dependent variations occurred predominantly close to the nozzle, where the shape and extent of regions with relatively cold mixtures changed; beyond $h \approx 20$ mm, variations were smaller. However, it must be kept in mind that the Raman measurements cover only the radial range up to $r = 27$ mm. The O_2, CO_2, and H_2O mole fraction

Fig. 8 Example of an instantaneous flow field from a single-shot PIV measurement displayed as streamline plot
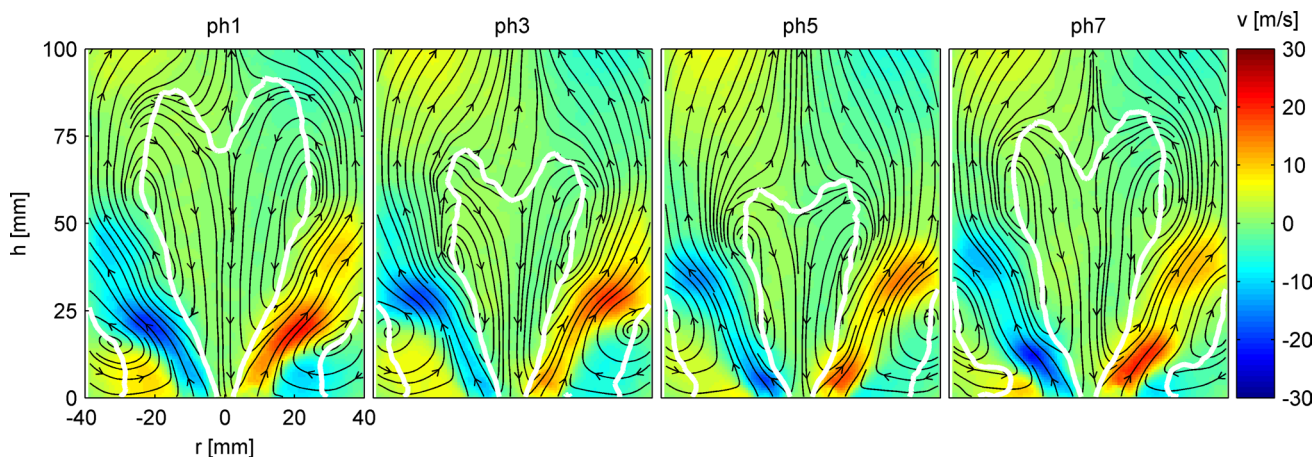
Fig. 9 Phase-correlated mean values of the flow field at phases 1, 3, 5, and 7. The radial velocity is color-coded. The white lines represent the shape of the recirculation zones (zero axial velocity)
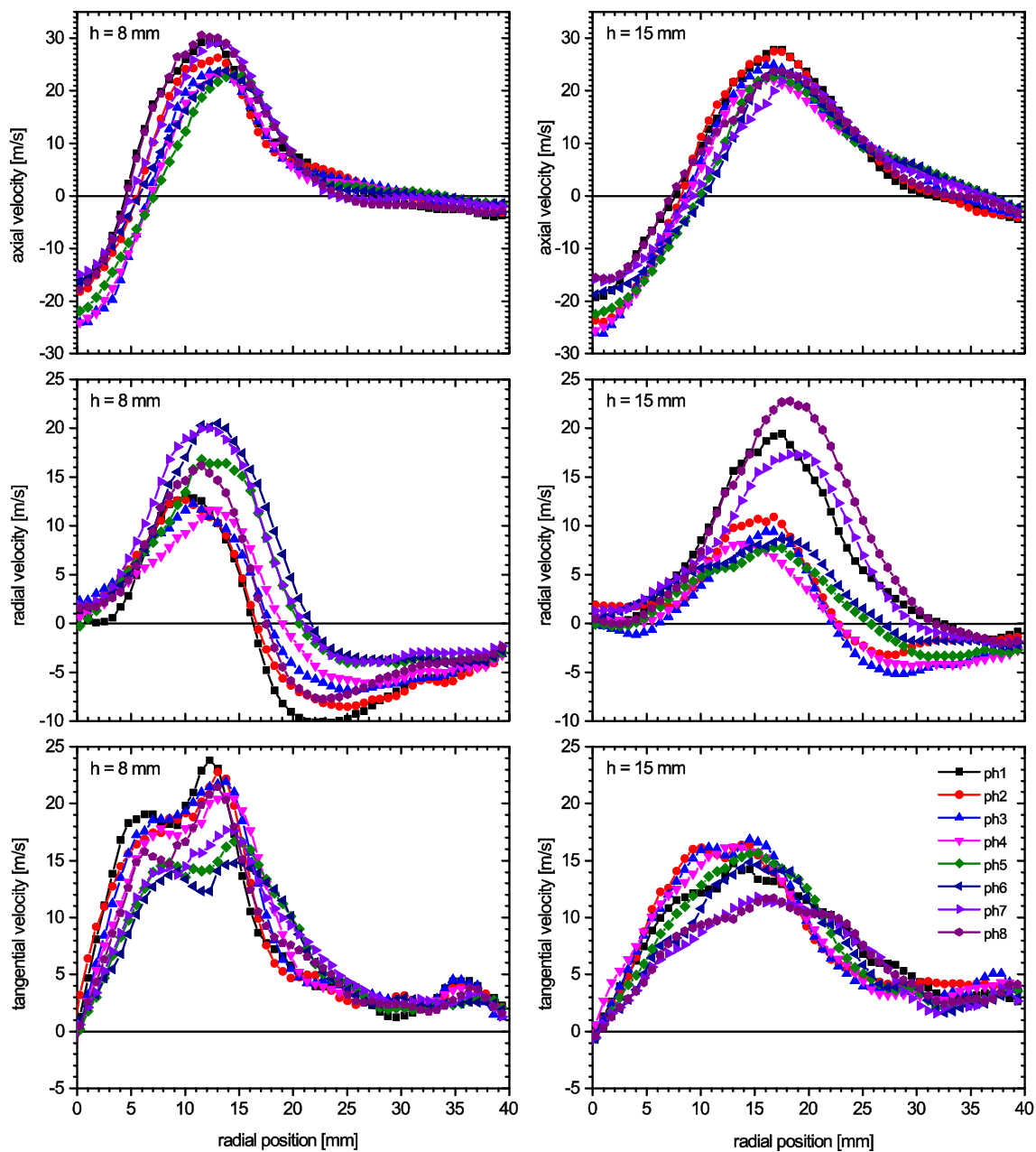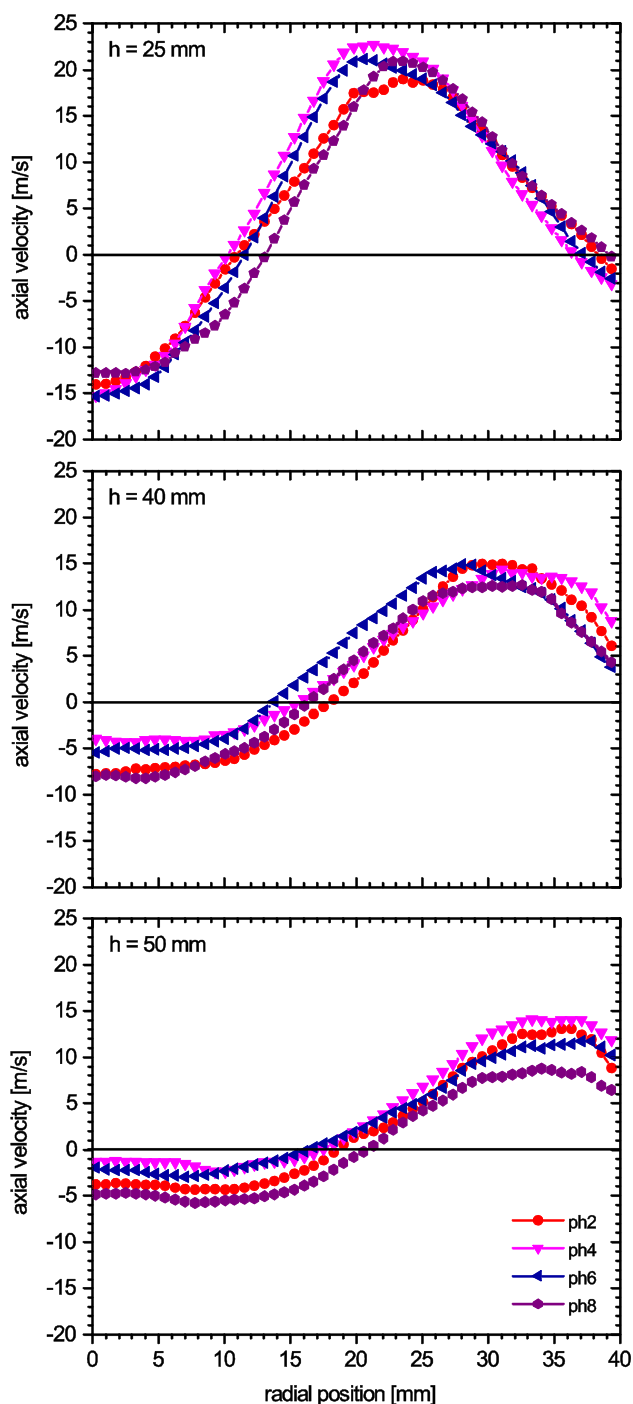
Fig. 10 Radial profiles of the phase-correlated mean values of the axial, radial, and tangential velocity components at $h = 8$ and 15 mm above the nozzle

distributions are in accordance with the temperature distributions and are not shown here.

A more detailed view of the phase-dependent variations is gained from the radial profiles of the phase-correlated mean values of the mixture fraction and temperature at $h = 8$ mm displayed in Fig. 13. In addition, the bars in the top left corner indicate the phase-dependent radial extent of the flame zone as determined from Fig. 5b. The mean mixture fraction is larger than the global mixture fraction ($\xi_{global} = 0.0391$) up to $r = 11$–14 mm and larger than the stoichiometric

mixture fraction ($\xi_{stoich.} = 0.055$) up to $r = 10$–12 mm (depending on the phase). This region corresponds to the IRZ and the inflow from the central nozzle that carries the fuel. For comparison, the average equivalence ratio deduced from the mass flow rates in the central nozzle is $\phi_i = 1.8$ ($\xi_i = 0.106$). The adjacent region, $r \approx 12$–20 mm, corresponds to the flow from the outer nozzle. Here, the mixtures are relatively lean, with $\bar{\xi} < \xi_{global}$. Beyond $r \approx 20$ mm is the region of the ORZ (negative radial velocity, see Fig. 11) where $\bar{\xi}$ is only slightly smaller than ξ_{global}.

Fig. 11 Radial profiles of the phase-correlated mean values of the axial velocity components at $h = 25$, 40, and 50 mm above the nozzle

Whereas $\bar{\xi}$ is hardly influenced by the thermo-acoustic oscillation in the ORZ, the phase-dependent variations are well pronounced in the central region. At ph1 and ph8, $\bar{\xi}$ and the radial extent of the fuel-rich region were at their respective maxima. The minima were reached around ph4. The comparison with the radial spread of the flame zone

may suggest that the extent of the flame zone is larger when $\bar{\xi}$ is close to $\xi_{stoich.}$. However, a more detailed inspection is needed to associate the presence of a flame with the local thermo-chemical state and flow field (see below). The RMS values (not shown) roughly followed the trend of the mean values, but the phase-dependent variations were not as pronounced.
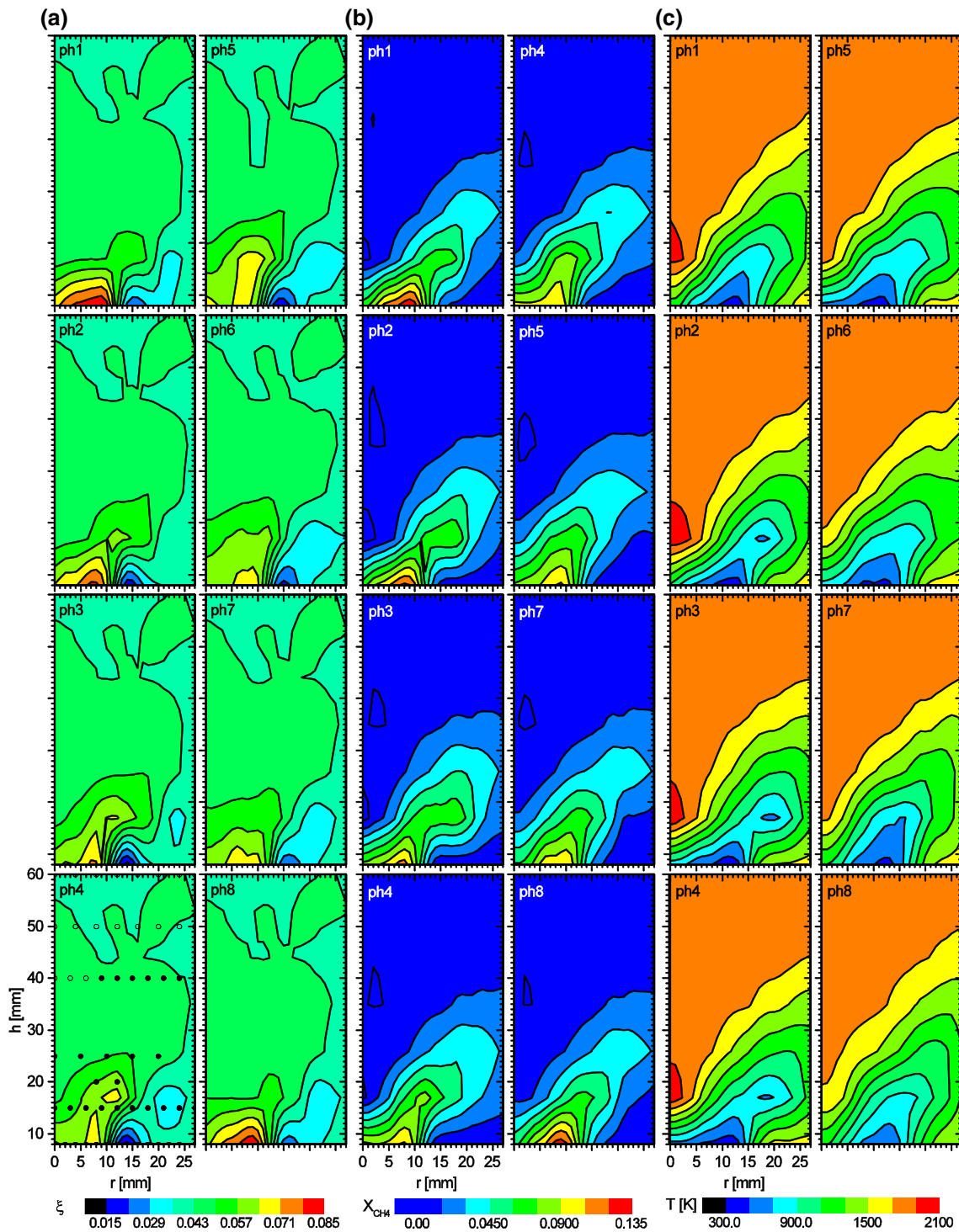
The profiles of the phase-correlated mean temperatures, $\overline{T}$, show the largest variations in the IRZ. The RMS temperature values (not shown here) of up to 660 K reflect the large fluctuations in the flame zone. Thus, the observed phase-dependent temperature variations can be caused by either intermittent combustion or by transport and mixing of burned and unburned gas.

Figure 14 shows the profiles of the mean values of the mixture fraction and temperature at $h = 15$ mm. Similar to $h = 8$ mm, mixtures with $\bar{\xi} > \xi_{global}$ were observed for $r < 16$–21 mm (depending on the phase) and $\bar{\xi} > \xi_{stoich.}$ at least for some phases and some radial locations. For all phases, $\bar{\xi}$ is close to $\xi_{stoich.}$ up to $r \approx 15$ mm. This region corresponds well with the radial spread of the flame zone indicated by the bars. Like at $h = 8$ mm, large RMS values of the temperature of up to 650 K are encountered within the flame zone. Significant phase-dependent temperature variations are present, particularly in the IRZ and the shear layer between the IRZ and the inflow, i.e., the region of the flame zone. At this height, the maximum heat release is at ph5 and ph6, the minimum at ph1 and ph2. There are relationships between the phase-dependent profiles of $\bar{\xi}$ and $\overline{T}$ and the size and intensity of the flame; however, the situation is complex and cannot be fully answered by mean values. Therefore, correlations between temperature and mixture fraction are considered in the following section.

3.5 Variations in thermo-chemical states

In partially premixed turbulent combustion, the stabilization of a flame front requires thermo-chemical conditions that enable a "fast" flame chemistry and a flow field with locally low strain rates. With respect to chemistry, near-stoichiometric mixtures and elevated mixture temperatures are favorable for flame stabilization. To assess the thermo-chemical state of the flame investigated, Fig. 15 shows scatterplots of temperature versus mixture fraction at $h = 8$ and 15 mm. Here, the samples from all phases and radial measurement locations have been combined in one plot (a phase-correlated analysis of single-shot results is beyond the scope of this paper). Each dot represents the result of a single-shot measurement, and results from different radial locations are marked by different colors. For comparison, the solid line represents the thermo-chemical state at adiabatic equilibrium. The vertical dashed lines indicate ξ_{global} and $\xi_{stoich.}$. It is noted that due to the turbulent fluctuations,

Fig. 12 2D distributions of the phase-correlated mean values of **a** mixture fraction, **b** CH$_4$ mole fraction, and **c** temperature. The plots have been generated from the Raman point measurements by interpolation. *Open symbols* in the plot of ph4 of subfigure (**a**) are the non-phase-correlated measurement locations, and *closed symbols* are the phase-correlated measurement locations
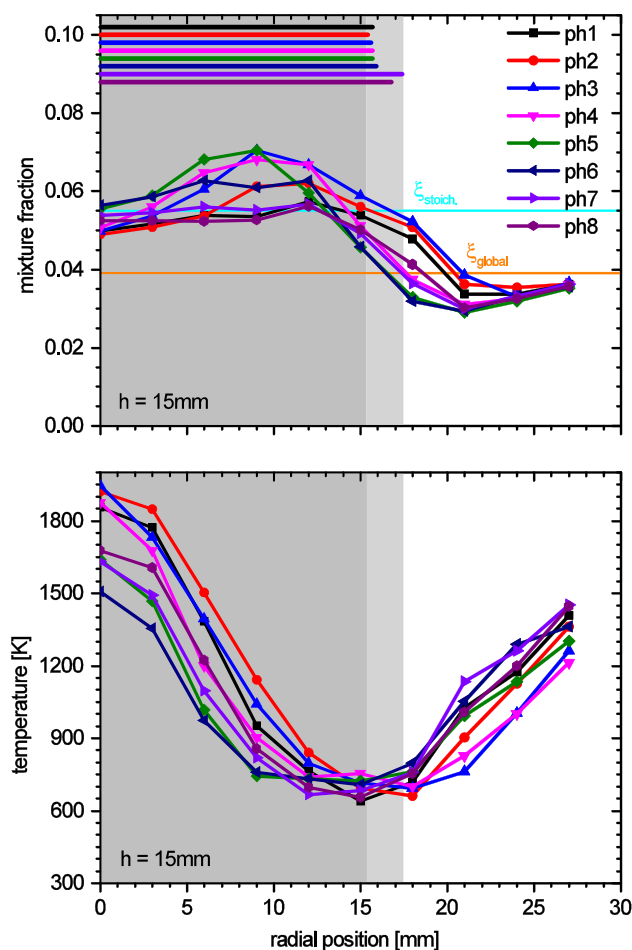
the attribution of the samples to certain flow regions is not strict. The samples from the outer radial locations ($r \geq 22$ mm for $h = 8$ mm, $r \geq 24$ mm for $h = 15$ mm, green dots) are predominantly from the ORZ. They are

close to ξ_{global}, and the observed scatter in mixture fraction is largely caused by the measurement precision. The measured temperatures are slightly below the adiabatic flame temperature. An inspection of the species concentrations
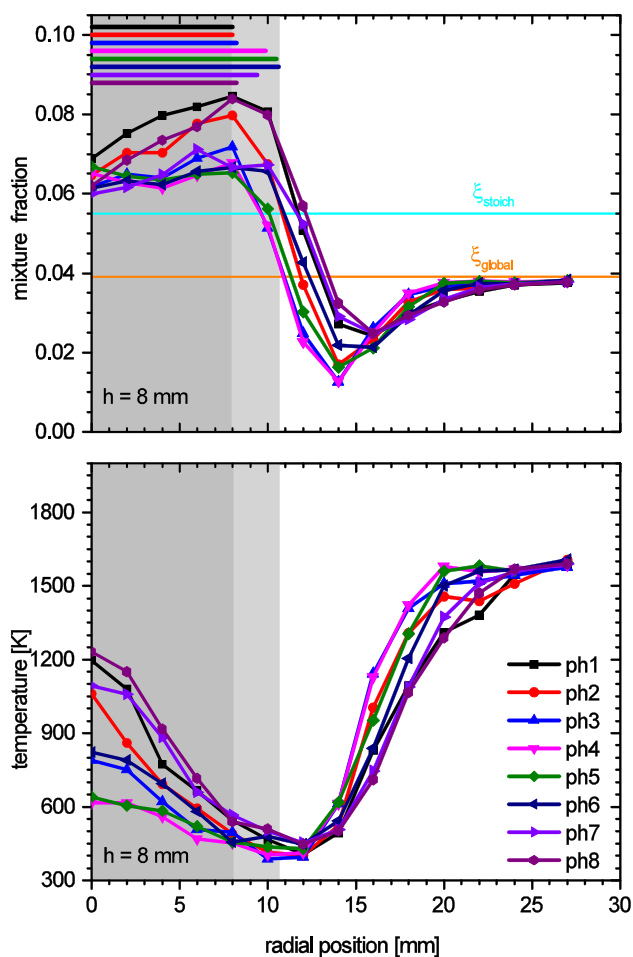
Fig. 13 Radial profiles of the phase-correlated mean values of the mixture fraction and temperature for eight phases at $h = 8$ mm. Shown in the upper left corner is the phase-averaged radial extent of the reaction zone, determined from the deconvoluted OH* CL images in Fig. 5b. As an additional guide to the eye, the gray-shaded areas represent the flame zone: *dark gray* is the zone with a flame for all phase angles, *light gray* is the zone with a flame only for certain phase angles

Fig. 14 Radial profiles of the phase-correlated mean values of the mixture fraction and temperature for eight phases at $h = 15$ mm. Shown in the upper left corner is the phase-averaged radial extent of the reaction zone, determined from the deconvoluted OH* CL images in Fig. 5b. As an additional guide to the eye, the gray-shaded areas represent the flame zone: *dark gray* is the zone with a flame for all phase angles; *light gray* is the zone with a flame only for certain phase angles

shows that the flame is near chemical equilibrium in this region; the temperature decrease relative to the adiabatic equilibrium is most likely caused by heat loss of the combustion gases at the burner plate and the combustor walls during the transport in the ORZ. The samples in the adjacent radial region present mixtures of the gas from the ORZ and the air from the outer nozzle (outer shear layer, orange dots). The radial regions between $r \approx 6$ and 10 mm for $h = 8$ mm and $r \approx 9$ and 15 mm for $h = 15$ mm represent the inflowing fresh gas and its shear layer with the IRZ (blue dots). Here, the scatter in mixture fraction is particularly large. Finally, the samples from the radial region around $r = 0$ mm stem mostly from the IRZ (red dots). Their mixture fraction lies between ξ_{global} and $\xi_{stoich.}$, and the temperatures are close to the adiabatic temperature.

Many samples exhibit intermediate temperatures between room temperature and adiabatic flame temperature, and mixture fractions between ξ_{global} and $\xi \approx 0.15$. The corresponding distributions of species concentrations revealed that these samples contain CH_4, air, and exhaust gas. The majority of them represent mixtures of exhaust gas from the IRZ and fresh fuel/air mixtures from the inner nozzle, which have not reacted yet due to ignition delay. Such behavior has often been observed in flames with recirculating burned gas (Gregor et al. 2009; Kojima and Fischer 2013; Masri et al. 2004; Meier et al. 2006; Stopper et al. 2013; Sweeney et al. 2012; Wehr et al. 2007) and an estimation of the ignition delay times with the timescale of the flow field in a similar burner supports this interpretation (Meier et al. 2006). The thermo-chemical states of
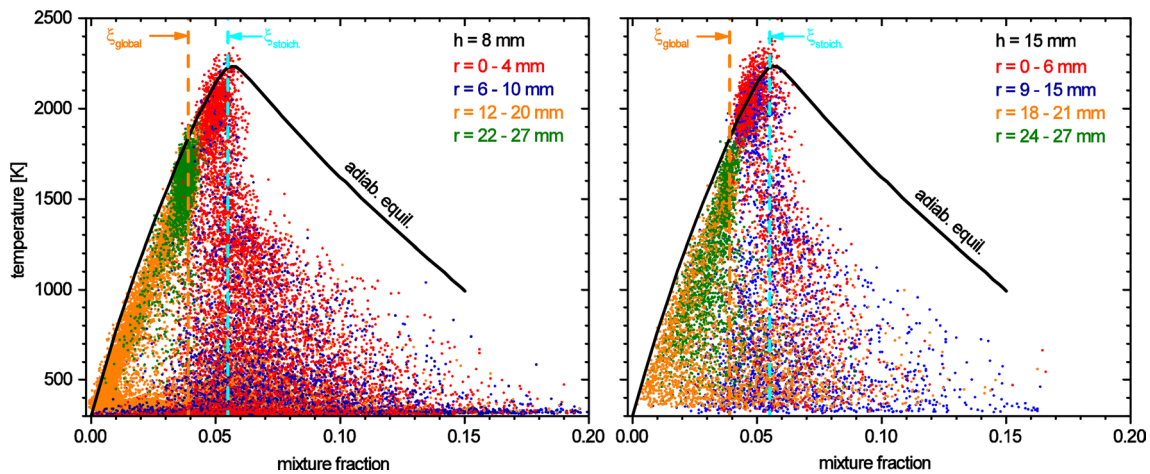
Fig. 15 Scatterplots of mixture fraction versus temperature for $h = 8$ and 15 mm. Color-coded is the radial position of the samples; the *orange vertical line* corresponds to the global mixture fraction and the *cyan vertical line* to the stoichiometric mixture fraction. Also shown is the adiabatic equilibrium for 350 K fresh gas temperature with a strain rate of 1/s at 1 bar

these samples with elevated temperatures and near-stoichiometric compositions provide optimal conditions for flame stabilization. Thus, it is not surprising that their radial locations coincide with those of the flame zones for the respective heights.

With respect to the local flow field, it must be considered that it is not possible to perform Raman and PIV measurements simultaneously; the single-shot samples from the scatterplots cannot be assigned to an instantaneous velocity. Therefore, the mean and RMS values of the velocity are examined. Within the radial expansion of the flame zone, the mean axial velocity varies between $\bar{u}'' \approx -25$ and 25 m/s (see Fig. 10) with RMS fluctuations in the range of $u'' = 10$–20 m/s (not displayed). Thus, regions with low velocity and low local strain rates are expected to be found in this region. This is confirmed by the inspection of single-shot velocity distributions like the one displayed in Fig. 8.

During a cycle of the thermo-acoustic oscillation, the flow field and the scatterplots do not change fundamentally, i.e., samples with elevated temperatures and near-stoichiometric mixtures are always present in the radial region of the IRZ and the shear layer between the IRZ and the inflow from the inner nozzle. Therefore, the stabilization region and the flame shape do not change significantly during an oscillation cycle. However, the total rate of heat release varies, particularly further downstream as seen from Fig. 6.

Figure 16 displays radial profiles of the phase-correlated mean values (Reynolds-averaged) of $\overline{X}_{CH_4}$ at $h = 8$ and 15 mm. The phase-dependent variations manifest in the maximum mole fractions being reached at different phases, and in the radial extent over which CH_4 was found. The phase at which the maximum CH_4 mole fraction and radial extent were reached changed with downstream distance between $h = 8$ and 15 mm; whereas the maximum

was reached at around ph8 and ph1 for $h = 8$ mm, it shifted to approximately ph3 at $h = 15$ mm. This reflects the convective transport of fuel that was already observed in the 2D plots of Fig. 12. Comparison of the $\overline{X}_{CH_4}$ profiles with those of the axial velocity (Fig. 10) shows that the velocity maxima lie at higher r than the $\overline{X}_{CH_4}$ maxima. This might be explained by the influence of the air flow from the outer nozzle that contributes to the flow field but not to the fuel concentration. At $h = 25$ mm, the peak mole fractions are reduced to approximately 0.04 (see Fig. 12b), mainly due to mixing and, to a lesser extent, by combustion because the majority of the heat release takes place above $h = 25$ mm.
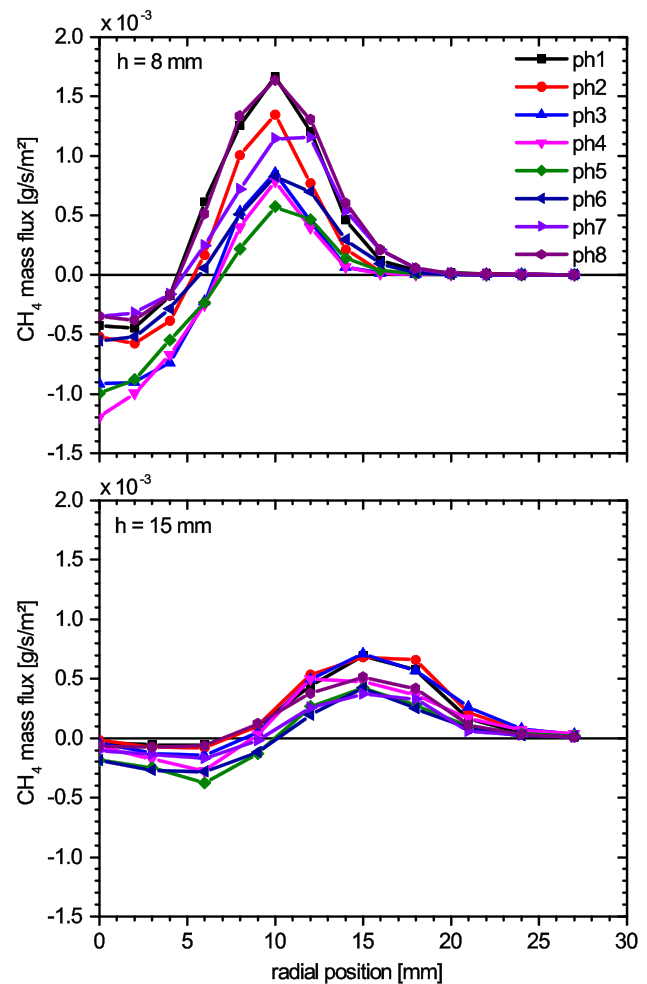
3.6 Variations in mass flow

The change in fuel mass flow through successive cross-sectional planes of the combustion chamber in the streamwise direction represents the fuel consumption distribution and therefore the heat release distribution; changes in these distributions over the thermo-acoustic cycle are important for understanding the feedback loop. Here, the combined results from the Raman and PIV measurements can be used to estimate the mass flows and their variations. With the knowledge of the axial velocity, density ρ, and mass fraction Y_i of a species i, the mass flux Φ_i (mass flow per area) through a cross-sectional plane is defined as $\Phi_i = \rho \cdot Y_i \cdot u = \rho_i \cdot u$. For a correct calculation, the product should be calculated on a single-shot basis. However, the PIV and Raman measurements have not been taken simultaneously, and thus, the mean flux is here approximated by a calculation based on the phase-dependent mean values. More precisely, the correct mean value of $\bar{\Phi}_i$ within a series of single-shot measurements is $\bar{\Phi}_i = (\Sigma \rho_{i,j} \cdot u_j)/N$, where the summation is over all single shots from $j = 1 - N$. The approximation is
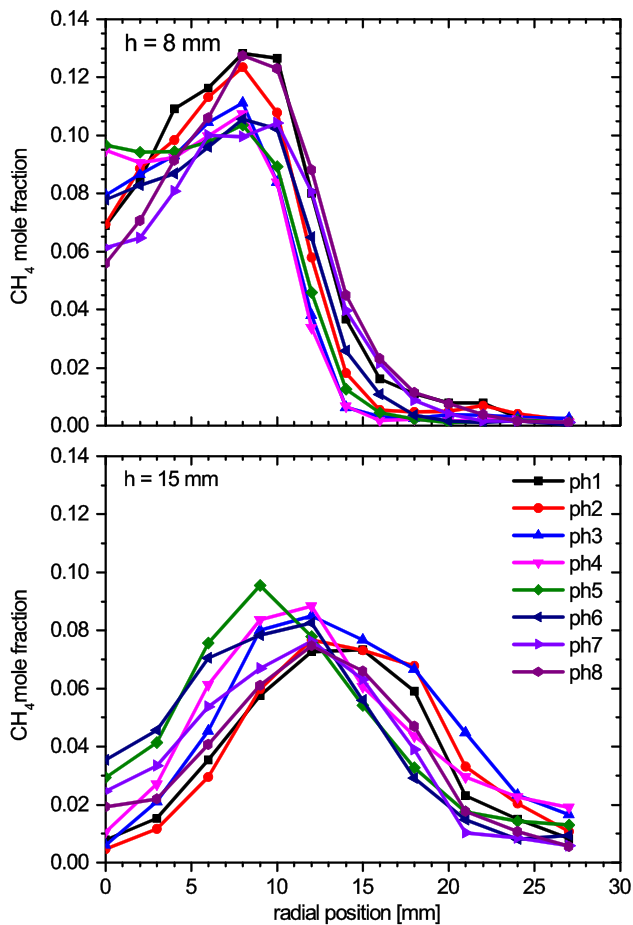
Fig. 16 Radial profiles of the phase-correlated mean values: the CH_4 mole fraction for eight phases at $h = 8$ and 15 mm

**Fig. 17** Radial profiles of the phase-correlated CH_4 flux through the cross-sectional planes at $h = 8$ and 15 mm

$\bar{\Phi}_i \approx (\Sigma\rho_{i,j} \cdot \Sigma u_j)/N^2 = \bar{\rho}_i \cdot \bar{u}$, where $\bar{\rho}_i$ and $\bar{u}$ are known from the Raman and PIV measurements, respectively. The approximation can lead to an error in regions where u depends on the gas composition, i.e., where u and ρ are not statistically independent. However, the main contribution to the CH_4 fluxes through the planes at $h = 8$ and 15 mm is from the inflow where the approximation should yield reasonable results. Furthermore, cylindrical symmetry of the flame was assumed for the determination of $\bar{\Phi}_i$.

Figure 17 shows radial profiles of the calculated phase-correlated mean mass flux of CH_4, $\bar{\Phi}_{CH_4} = \bar{\rho} \cdot \overline{Y}_{CH_4} \cdot \bar{u}$, through the planes at $h = 8$ and 15 mm. These profiles evidence the drastic variations in the fuel flow during an oscillation cycle and demonstrate the phase-dependent changes in a much clearer way than the profiles of velocity and mole fractions. It is noted that the total mass flow through a cross-sectional plane of the combustor is obtained by integration of the flux over the area. Therefore, the flux at a larger r contributes stronger to the total mass flow, while the mass flow close to the axis is relatively small.
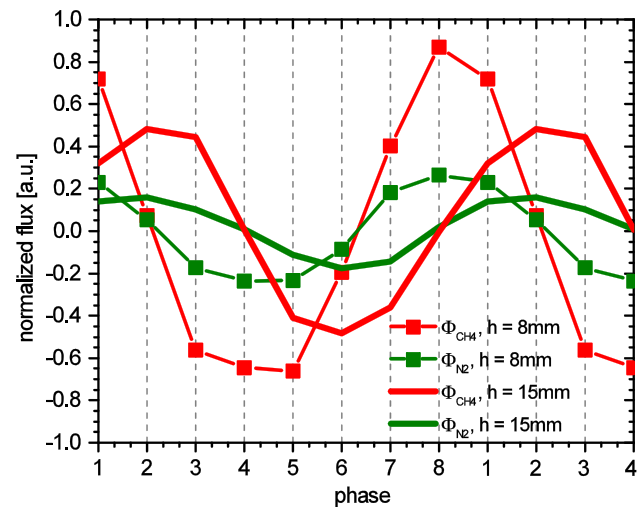
The total phase-averaged fuel flux is defined as $\{\bar{\Phi}_{CH_4}\} = \int \bar{\Phi}_{CH_4}(r)\mathrm{d}r$. Here, it was approximated by summing over all values displayed in Fig. 17. Figure 18 shows the normalized total phase-averaged flux $\left(\{\bar{\Phi}\} - \{\overline{\overline{\Phi}}\}\right)/\{\overline{\overline{\Phi}}\}$ for $h = 8$ mm. In addition to the flux of CH_4, some additional normalized fluxes are displayed for comparison. The normalized presentation enables a better comparison of the modulation amplitude. The volume flux, $\bar{\Phi}_V = \bar{u}$ (blue curve), is the calculated flux assuming constant density of the gas, i.e., assuming that phase-dependent variations are solely due to variations in the axial velocity. It varies by ± 16 % during an oscillation cycle, and the minimum and maximum value is reached at ph4 and ph8, respectively. Next, the influence of the temperature variations is included in the pink curve, which represents a "mass flux," $\bar{\Phi}_m = \bar{\rho} \cdot \bar{u}$; this includes phase-dependent variations in axial velocity and temperature (and thus density). However, here $\rho = \rho(T)$ is a function of the temperature only and does not include specific species
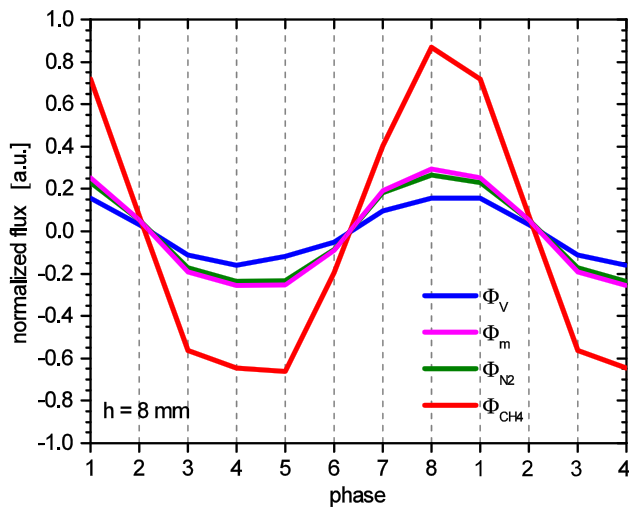
Fig. 18 Total fluxes of CH_4 and N_2 through the cross-sectional planes at $h = 8$ mm during an oscillation cycle. The *blue curve* (termed Φ_V) corresponds to the flux based on the axial velocity magnitude and represents the volume flux; the *pink curve* (termed Φ_m) includes the influence of the gas temperature and thus represents a "mass flux." The *green curve* (termed Φ_{N_2}) includes the influence of the gas temperature and composition and represents the N_2 mass flux. Additionally, the *red curve* (termed Φ_{CH_4}) represents the CH_4 mass flux

Fig. 19 Total fluxes of CH_4 and N_2 through the cross-sectional planes at $h = 8$ and 15 mm during an oscillation cycle. The fluxes include the influence of gas temperature and composition

concentrations. The mass flux has a similar phase dependence as the volume flux, but a greater oscillation amplitude (between -26 and $+29$ %). This means that high axial velocities are correlated with low temperatures. Next, the green curve shows the phase-dependent variations in the N_2 mass flux, $\bar{\Phi}_{N_2} = \bar{\rho} \cdot \bar{Y}_{N_2} \cdot \bar{u}$. It coincides almost with the curve of the mass flux $\bar{\Phi}_m$ and varies between -24 and $+26$ %. This is not surprising because the N_2 flux is mainly driven by the phase-dependent variations in the temperature and axial velocity, i.e., by the bulk air flow rate. Finally, the red curve shows the CH_4 mass flux, $\bar{\Phi}_{CH_4} = \bar{\rho} \cdot \bar{Y}_{CH_4} \cdot \bar{u}$. It exhibits the same phase dependence as the other curves, but an oscillation amplitude between -66 and $+87$ %. This means that the CH_4 mass flux is strongly influenced by the phase-dependent variation in the CH_4 concentrations. The similarity of the curves indicates that the variations in axial velocity, temperature, and CH_4 concentration interfere constructively, and that the total variation in fuel flux cannot be attributed to a single quantity.

Figure 19 shows the comparison of the (normalized) N_2 and CH_4 mass fluxes at $h = 8$ and 15 mm as a function of the phase. The strong variations in the CH_4 flux by almost 90 % at $h = 8$ mm diminished at $h = 15$ mm to approximately 48 %, predominantly due to mixing. Similarly, the variation in the N_2 flux also diminished at $h = 15$ mm; however, the difference in fluxes at the two heights for N_2 is less pronounced than for CH_4, since the N_2 flux is less influenced by mixing. It is seen that the traces at $h = 15$ mm

are shifted in phase compared to those at $h = 8$ mm, and that the shift is less during the increasing flux (positive slope) than during the decreasing flux (negative slope). For CH_4, the shift is approximately 1.5 phases ($\approx 70°$) for the increasing slope. The shift is explained by the convective transport of the alternating layers with low and high fuel concentrations. With increasing downstream position, the maximum of the CH_4 flux is shifted further along the phase axis. Unfortunately, the fluxes could not be calculated for $h > 15$ mm because phase-correlated Raman measurements did not cover the complete relevant radial region. An estimation of the CH_4 flux at $h = 25$ mm showed that the maximum is reached between ph3 and ph4. In Fig. 6, it was shown that the maximum heat release occurred around ph4 at $h = 36$ mm. This is in good agreement with an extrapolation of the maximum CH_4 flux for this height and supports the concept that the convective transport of layers with high CH_4 concentrations is directly coupled with the variation in heat release.
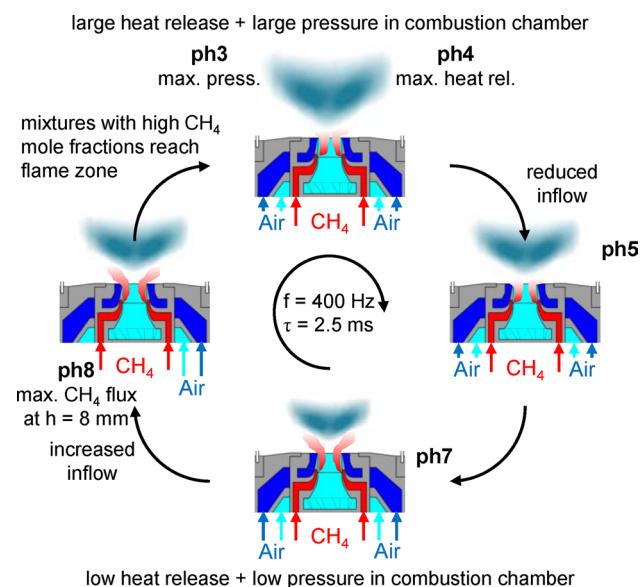
3.7 Feedback loop

In this section, a summary of the sequence of events during an oscillation cycle and the feedback mechanism of the thermo-acoustic instability will be presented; however, this is only meant as a qualitative description of the process. A quantity of decisive importance for the heat release is the convective transport of fuel to the flame zone. This is, however, not the only quantity that determines the heat release rate and its cyclic variations. Fluctuations in the flame surface area can be induced by periodic variations in the flow field, as was found in perfectly premixed configurations

(Balachandran et al. 2005; Caux-Brisebois et al. 2014). Although the fuel consumption remains the decisive quantity, phase-dependent characteristics of the flow field can trigger local changes in the fuel consumption rate. This is usually accompanied by a significant cyclic variation in the flame shape and position (Biagioli et al. 2008; Giezendanner et al. 2003; Meier et al. 2007). In the flame considered here, the cyclic change in flame shape was moderate, and the axial movement was small. Thus, the influence of velocity-coupled heat release variations is expected to be small, and the driving process for the observed heat release fluctuations was the varying fuel mass flux and the associated equivalence ratios.

Figure 20 illustrates the different phases during the cycle with cartoons, indicating the flow velocity in the central nozzle, the fuel distribution, and the flame zone. This feedback mechanism was described previously (Candel 2002; Dowling and Stow 2003; Huang and Yang 2009; Lieuwen and Yang 2005) and was observed in several different swirl burner geometries (Duan et al. 2005; Lieuwen and Zinn 1998; Meier et al. 2007). A determining quantity for this feedback mechanism is the pressure difference between the plenum and the combustion chamber. Because the amplitude of the pressure oscillations in the combustion chamber was much larger than in the air plenums, the pressure difference essentially followed the pressure trace in the combustion chamber. At the maximum pressure in the combustion chamber (ph3, $\alpha \approx 90°$), the acceleration of the flow within the central nozzle was at its minimum, and hence,

the axial velocity at the dump plane reached its smallest value shortly afterward. At the lowest available measurement position ($h = 2.5$ mm), the velocity profiles (not shown here) had their minima at ph4. This is also the phase at which the heat release reached its maximum. Because the fuel was injected with high momentum (relatively large pressure drop) into the central air nozzle, the fuel mass flow was less affected by the pressure variations in the combustion chamber. Therefore, mixtures with high CH_4 mole fractions built up in the central nozzle during the period of low air velocities around ph4.

With decreasing heat release and pressure in the combustion chamber, the flow velocity in the central nozzle increases. At $h = 2.5$ mm (not shown), the maximum velocities from the inner nozzle occur around ph8. This is confirmed by the velocity profiles at $h = 8$ mm. Together with the air flow from the central nozzle, the fuel-rich mixtures are convected into the combustion chamber. Accordingly, the local CH_4 mole fraction and mixture fraction increase. At $h = 8$ mm, the maximum values of $\bar{\xi}$ and $\bar{X}_{CH4}$ as well as $\bar{\Phi}_{CH4}$ are reached at around ph8, or approximately 1.25 ms after the buildup of the fuel-rich mixtures at ph4 in the nozzle. The corresponding mean convection velocity from $h = -12$ to 8 mm is ≈ 16 m/s and is in good agreement with the level of the axial velocity measured at $h = 2.5$ mm (≈ 14 m/s).

The layers of high fuel concentration were further convected downstream, while getting leaner due to mixing, and finally burned in the flame zone. Here, $\bar{\xi}$ was close to $\xi_{stoich.}$ or below, depending on the downstream position (see Fig. 13). It was shown that the decrease in CH_4 correlated well with the shape of the flame zone measured by OH* chemiluminescence. Because the heat release rate reached the maximum around ph4, the duration between the occurrence of maximum CH_4 mole fractions at $h = 8$ mm (ph8) and their arrival and consumption in the flame zone can be estimated to be approximately 180° phase angle or 1.25 ms. Considering that the axial location of the maximum heat release was $h \approx 35$ mm, a convective time of 1.25 ms between $h = 8$ and 35 mm corresponds to a mean axial velocity of $u \approx 22$ m/s. This value of the velocity agrees well with the measured axial velocity in this region. Finally, the increase in the heat release was coupled to the pressure increase in the combustion chamber that reaches its maximum at ph3, and the cycle began again.

Thus, the feedback mechanism observed in the present setup is based on a fuel flow rate and equivalence ratio oscillation coupled with a convective time delay, as previously described in the literature (Ćosić et al. 2015; Lieuwen and Yang 2005; Meier et al. 2007; Sattelmayer 2003; Schürmans et al. 2004). If the convective time delay between the locations of the fuel injection and heat release is in (near) resonance with the period of an acoustic mode

Fig. 20 Schematic presentation of the feedback loop. The mechanism observed in the present measurements is consistent with the one described in the literature (Lieuwen and Zinn 1998; Lieuwen and Yang 2005)

of the combustion system, periodic pressure oscillations can sustain themselves. It is noted that the characterization of the feedback mechanism given here is not meant as a quantitative description. Details of the sequence of events and a quantitative analysis are left to numerical simulations, which are able to characterize the mixing process even at those locations that are not accessible for optical techniques, e.g., inside the central nozzle.

4 Summary and conclusions

A gas turbine model combustor was designed and set up for the investigation of thermo-acoustic combustion instabilities within the framework of the German Research Foundation Collaborative Research Center 606. In the current study, the dominant thermo-acoustic instability at approximately 400 Hz in a partially premixed flame with a global equivalence ration of 0.7 and a thermal power of 25 kW was studied at atmospheric pressure. This oscillation corresponded to a resonance of the system where half the wavelength matched the length of the inner plenum. Measurements of OH* chemiluminescence, flow field, major species concentrations, mixture fraction, and temperature were taken and off-line phase-correlated to the pressure oscillations in the combustion chamber.

The pressure variations in the combustion chamber affected the flow field in different ways. In addition to pronounced variations in the velocity of the inflowing jet, the inner recirculation zone varied in size and strength, particularly downstream of the flame zone. This variation was initiated by the oscillating heat release rate and the corresponding oscillating thermal expansion that caused a variation in the axial momentum and swirl number. The flame shape did not change much during an oscillation cycle; however, the OH* chemiluminescence intensity varied significantly.

At the lowest axial position of the Raman measurements ($h = 8$ mm), the mixtures were on the average fuel-rich in the central region up to $r \approx 10$ mm and fuel-lean further outside. This spatial distribution was caused by the nozzle arrangement and the fact that only the central nozzle carried the fuel. The region around the burner axis at $h \approx 8$ mm was the location where the flame was anchored. The radial spread of the flame zone at $h = 8$ and 15 mm was compared to the thermo-chemical state of the gas mixtures on the basis of single-shot Raman results. The frequent occurrence of near-stoichiometric mixtures with elevated temperatures explained why the flame resided in the specific regions.

The thermo-acoustic oscillations were accompanied by significant phase-dependent variations in the mixture fraction and fuel mole fraction in the inflowing jet and in the low part of the IRZ. Further up in the IRZ and in the ORZ, the variations were small, most likely because the residence time was long enough to balance out the cyclic variations observed in the inflow.

The phase-correlated mean fluxes of different molecular species through cross-sectional planes of the combustion chamber were approximated by combining the phase-correlated mean values of the axial velocity and species mass densities. At $h = 8$ mm, the CH_4 flux varied between -66 and $+87$ %, while the corresponding N_2 flux varied between -24 and $+26$ %. At $h = 15$ mm, the variations were reduced mainly due to the mixing progress. The observed phase shift of the fluxes between $h = 8$ and 15 mm showed how the fuel stratification convected downstream. The cyclic variations in the fuel flux and equivalence ratio were explained by the different response of the air and fuel flows to the pressure variations in the combustion chamber. While the air flow was injected with a pressure drop of $\Delta p_{air} \approx 1.5$ % across the nozzle, the pressure drop of the fuel injection was significantly larger ($\Delta p_{fuel} \approx 7.5$ %). In this way, mixtures with high fuel concentrations built up in the central nozzle during phases of a low air flow rate, which subsequently entered the combustion chamber and convected toward the flame zone. The experimental results were combined to a qualitative description of the sequence of events and the feedback loop that corresponds to a mechanism that can be summarized as equivalence ratio fluctuations with convective delay. This finding was in agreement with previous studies that observed the same feedback mechanism. It was shown that the convective delay of the fuel transport ($\tau \approx 2.5$ ms) corresponded to the oscillation period of a resonance of the combustor.

References

Allison PM, Driscoll JF, Ihme M (2012) Acoustic behavior of a partially-premixed gas turbine model combustor. In: Proceedings of the 50th AIAA Aerospace Sciences Meeting: AIAA 2012-0504

Arndt CM, Steinberg AM, Boxx IG, Meier W, Carter CD, Aigner M (2010) Flow-field and flame dynamics of a gas turbine model combustor during transition between thermo-acoustically stable and unstable states. In: Proceedings of the ASME Turbo Expo: GT2010-22830

Ayoola BO, Balachandran R, Frank JH, Mastorakos E, Kaminski CF (2006) Spatially resolved heat release rate measurements in turbulent premixed flames. Combust Flame 144:1–16

Bade S, Wagner M, Hirsch C, Sattelmayer T, Schuermans B (2014) Influence of fuel-air mixing on flame dynamics of premixed swirl burners. In: Proceedings of the ASME Turbo Expo: GT2014-25381

Balachandran R, Ayoola BO, Kaminski CF, Dowling AP, Mastorakos E (2005) Experimental investigation of the nonlinear response of turbulent premixed flames to imposed inlet velocity oscillations. Combust Flame 143:37–55

Bärow E, Koch R, Bauer H-J (2013) Comparison of oscillation modes of spray and gaseous flames. In: Proceedings of the Eighth Mediterranean Combustion Symposium: EGTSC-26

Bellows BD, Bobba MK, Seitzman JM, Lieuwen T (2007) Nonlinear flame transfer function characteristics in a swirl-stabilized combustor. J Eng Gas Turbines Power 129:954–961

Bergmann V, Meier W, Wolff D, Stricker W (1998) Application of spontaneous Raman and Rayleigh scattering and 2D LIF for the characterization of a turbulent $CH_4/H_2/N_2$ jet diffusion flame. Appl Phys B 66:489–502

Biagioli F, Güthe F, Schuermans B (2008) Combustion dynamics linked to flame behaviour in a partially premixed industrial burner. Exp Therm Fluid Sci 32:1344–1353

Bilger RW, Stårner SH, Kee RJ (1990) On reduced mechanisms for methane air combustion in nonpremixed flames. Combust Flame 80:135–149

Boxx I, Stöhr M, Carter C, Meier W (2010) Temporally resolved planar measurements of transient phenomena in a partially premixed swirl flame in a gas turbine model combustor. Combust Flame 157:1510–1525

Boxx I, Arndt CM, Carter CD, Meier W (2012) Highspeed laser diagnostics for the study of flame dynamics in a lean premixed gas turbine model combustor. Exp Fluids 52:555–567

Brockhinke A, Krüger J, Heusing M, Letzgus M (2012) Measurement and simulation of rotationally-resolved chemiluminescence spectra in flames. Appl Phys B 107:539–549

Bulat G, Jones WP, Marquis AJ (2013) Large Eddy Simulation of an industrial gas-turbine combustion chamber using the sub-grid PDF method. Proc Combust Inst 34:3155–3164

Candel S (2002) Combustion dynamics and control: progress and challenges. Proc Combust Inst 29:1–28

Candel S, Durox D, Schuller T, Bourgouin J-F, Moeck JP (2014) Dynamics of swirling flames. Ann Rev Fluid Dyn 46:147–173

Caux-Brisebois V, Steinberg AM, Arndt CM, Meier W (2014) Thermo-acoustic velocity coupling in a swirl stabilized gas turbine model combustor. Combust Flame 161:3166–3180

Ćosić B, Terhaar S, Moeck JP, Paschereit CO (2015) Response of a swirl-stabilized flame to simultaneous perturbations in equivalence ratio and velocity at high oscillation amplitudes. Combust Flame 162:1046–1062

Dem C, Stöhr M, Arndt CM, Steinberg AM, Meier W (2015) Experimental study of turbulence-chemistry interactions in perfectly and partially premixed confined swirl flames. Z Phys Chem. doi:10.1515/zpch-2014-0583

Dowling AP, Stow SR (2003) Acoustic analysis of gas turbine combustors. J Propuls Power 19:751–764

Duan XR, Meier W, Weigand P, Lehmann B (2005) Phase-resolved laser Raman scattering and laser doppler velocimetry applied to periodic instabilities in a gas turbine model combustor. Appl Phys B 80:389–396

Durox D, Moeck JP, Bourgouin J-F, Morenton P, Viallon M, Schuller T, Candel S (2013) Flame dynamics of a variable swirl number system and instability control. Combust Flame 160:1729–1742

Franzelli B, Riber E, Gicquel LYM, Poinsot T (2012) Large Eddy Simulation of combustion instabilities in a lean partially premixed swirled flame. Combust Flame 159:621–637

Fritsche D, Füri M, Boulouchos K (2007) An experimental investigation of thermoacoustic instabilities in a premixed swirl-stabilized flame. Combust Flame 151:29–36

Galley D, Ducruix S, Lacas F, Veynante D (2011) Mixing and stabilization study of a partially premixed swirling flame using laser induced fluorescence. Combust Flame 158:155–171

Gicquel LYM, Staffelbach G, Poinsot T (2012) Large Eddy Simulations of gaseous flames in gas turbine combustion chambers. Prog Energy Combust Sci 38:782–817

Giezendanner R, Keck O, Weigand P, Meier W, Meier U, Stricker W, Aigner M (2003) Periodic combustion instabilities in a swirl burner studied by phase-locked planar laser-induced fluorescence. Combust Sci Technol 175:721–741

Gounder JD, Boxx I, Kutne P, Wysocki S, Biagioli F (2014) Phase resolved analysis of flame structure in lean premixed swirl flames of a fuel staged gas turbine model combustor. Combust Sci Technol 186:421–434

Gregor MA, Seffrin F, Fuest F, Geyer D, Dreizler A (2009) Multi-scalar measurements in a premixed swirl burner using 1D Raman/Rayleigh scattering. Proc Combust Inst 32:1739–1746

Gupta AK, Lilley DG, Syred N (1984) Swirl flows. Abacus Press, Kent

Haber LC, Vandsburger U (2003) A global reaction model for OH* chemiluminescence applied to a laminar flat-flame burner. Combust Sci Technol 175:1859–1891

Hardalupas Y, Panoutsos CS, Taylor AMKP (2010) Spatial resolution of a chemiluminescence sensor for local heat-release rate and equivalence ratio measurements in a model gas turbine combustor. Exp Fluids 49:883–909

Hermeth S, Staffelbach G, Gicquel LYM, Anisimov V, Cirigliano C, Poinsot T (2014) Bistable swirled flames and influence on flame transfer functions. Combust Flame 161:184–196

Huang Y, Yang V (2009) Dynamics and stability of lean-premixed swirl-stabilized combustion. Prog Energy Combust Sci 35:293–364

Hubschmid W, Bombach R, Inauen A, Güthe F, Schenker S, Tylli N, Kreutner W (2008) Thermoacoustically driven flame motion and heat release variation in a swirl-stabilized gas turbine burner investigated by LIF and chemiluminescence. Exp Fluids 45:167–182

Im SH (2012) Caractérisation des instabilités thermoacoustiques dans les chambres de combustion à gaz, Master Thesis, École Centrale Paris

Ishino Y, Hasegawa T, Yamaguchi S, Ohiwa N (2001) Optical analysis of pulse combustion using shadowgraph and planar CH-LIF imaging technique. J Energy Resour Technol 123:59–63

Keck O, Meier W, Stricker W, Aigner M (2002) Establishment of a confined swirling natural gas/air flame as a standard flame: temperature and species distributions from laser Raman measurements. Combust Sci Technol 174:117–151

Kim M-K, Yoon J, Oh J, Lee J, Yoon Y (2014) An experimental study of fuel–air mixing section on unstable combustion in a dump combustor. Appl Therm Eng 62:662–670

Kojima JJ, Fischer DG (2013) Multiscalar analyses of high-pressure swirl-stabilized combustion via single-shot dual-SBG Raman spectroscopy. Combust Sci Technol 185:1735–1761

Komarek T, Polifke W (2010) Impact of swirl fluctuations on the flame response of a perfectly premixed swirl burner. J Eng Gas Turbines Power 132:061503

Kraus C, Bockhorn H (2013) Experimental and numerical investigation of combustion instabilities in swirl-stabilized flames operated in partially-premixed mode. In: Proceedings of the European Combustion Meeting: P5-26

Lartigue G, Meier U, Bérat C (2004) Experimental and numerical investigation of self-excited combustion oscillations in a scaled gas turbine combustor. Appl Therm Eng 24:1583–1592

Lawson NJ, Wu J (1997) Three-dimensional particle image velocimetry: experimental error analysis of a digital angular stereoscopic system. Meas Sci Technol 8:1455–1464

Lee JG, Santavicca DA (2003) Experimental diagnostics for the study of combustion instabilities in lean premixed combustors. J Propuls Power 19:735–750

Lieuwen TC (2012) Unsteady combustor physics. Cambridge University Press, New York

Lieuwen TC, Yang V (2005) Combustion instabilities in gas turbine engines: operational experience, fundamental mechanisms, and modeling. American Institute of Aeronautics and Astronautics Inc, Reston

Lieuwen T, Zinn BT (1998) The role of equivalence ratio oscillations in driving combustion instabilities in low NO_x gas turbines. Symp Int Combust 27:1809–1816

Lilley DG (1977) Swirl flows in combustion: a review. AIAA J 15:1063–1078

Lückerath R, Lammel O, Stöhr M, Boxx I, Stopper U, Meier W, Janus B, Wegner B (2011) Experimental investigations of flame stabilization of a gas turbine combustor. In: Proceedings of the ASME Turbo Expo: GT2011-45790

Masri AR (2015) Partial premixing and stratification in turbulent flames. Proc Combust Inst 35:1115–1136

Masri AR, Kalt PAM, Barlow RS (2004) The compositional structure of swirl-stabilised turbulent nonpremixed flames. Combust Flame 137:1–37

Meier W, Duan XR, Weigand P (2006) Investigations of swirl flames in a gas turbine model combustor II. Turbulence-chemistry interactions. Combust Flame 144:225–236

Meier W, Weigand P, Duan XR, Giezendanner-Thoben R (2007) Detailed characterization of the dynamics of thermoacoustic pulsations in a lean premixed swirl flame. Combust Flame 150:2–26

Moeck JP, Bourgouin J-F, Durox D, Schuller T, Candel S (2012) Nonlinear interaction between a precessing vortex core and acoustic oscillations in a turbulent swirling flame. Combust Flame 159:2650–2668

Oberleithner K, Stöhr M, Im SH, Arndt CM, Steinberg AM (2015) Formation and flame-induced suppression of the precessing vortex core in a swirl combustor: experiments and linear stability analysis. Combust Flame. doi:10.1016/j.combustflame.2015.02.015

Palies P, Durox D, Schuller T, Candel S (2010) The combined dynamics of swirler and turbulent premixed swirling flames. Combust Flame 157:1698–1717

Palies P, Schuller T, Durox D, Gicquel L-YM, Candel S (2011) Acoustically perturbed turbulent premixed swirling flames. Phys Fluids 23:037101

Poinsot R, Veynante D (2012) Theoretical and numerical combustion, 3rd edn

Rebosio F, Widenhorn A, Noll B, Aigner M (2010) Numerical simulation of a gas turbine model combustor operated near the lean extinction limit. In: Proceedings of the ASME Turbo Expo: GT2010-22751

Reichling G, Noll B, Aigner M (2013) Numerical simulation of the non-reactive and reactive flow in a swirled model gas turbine combustor. In: Proceedings of the 21st AIAA Computational Fluid Dynamics Conference: AIAA-2013-2434

Renaud A, Ducruix S, Scouflaire P, Zimmer L (2015) Flame shape transition in a swirl stabilised liquid fueled burner. Proc Combust Inst 35:3365–3372

Reuer N (2013) Numerische Simulation der Akustik eines Gasturbinen-Modellbrenners, Bachelor Thesis, University of Stuttgart

Sadanandan R, Meier W, Heinze J (2012) Experimental study of signal trapping of OH laser induced fluorescence and chemiluminescence in flames. Appl Phys B 106:717–724

Sattelmayer T (2003) Influence of the combustor aerodynamics on combustion instabilities from equivalence ratio fluctuations. J Eng Gas Turbines Power 125:11–19

Schadow KC, Gutmark E (1992) Combustion instability related to vortex shedding in dump combustors and their passive control. Prog Energy Combust Sci 18:117–132

Schildmacher K-U, Koch R, Bauer H-J (2006) Experimental characterization of premixed flame instabilities of a model gas turbine burner. Flow Turbul Combust 76:177–197

Schuller T, Durox D, Candel S (2003) Self-induced combustion oscillations of laminar premixed flames stabilized on annular burners. Combust Flame 135:525–537

Schürmans B, Bellucci V, Güthe F, Meili F, Flohr P, Paschereit CO (2004) A detailed analysis of thermoacoustic interaction mechanisms in a turbulent premixed flame. In: Proceedings of the ASME Turbo Expo: GT2004-53831

See YC, Ihme M (2014) LES investigation of flow field sensitivity in a gas turbine model combustor. In: Proceedings of the 52nd AIAA Aerospace Sciences Meeting: AIAA 2014-0621

See YC, Ihme M (2015) Large eddy simulation of a partially-premixed gas turbine model combustor. Proc Combust Inst 35:1225–1234

Severin MJ (2012) Experimentelle Untersuchung der Verbrennungsinstabilitäten eines Gasturbinen-Modellbrenners. Diploma Thesis, University of Stuttgart

Steinberg AM, Boxx I, Stöhr M, Carter CD, Meier W (2010) Flow-flame interactions causing acoustically coupled heat release fluctuations in a thermo-acoustically unstable gas turbine model combustor. Combust Flame 157:2250–2266

Steinberg AM, Boxx I, Stöhr M, Meier W, Carter CD (2012) Effects of flow structure dynamics on thermoacoustic instabilities in swirl-stabilized combustion. AIAA J 50:952–967

Steinberg AM, Arndt CM, Meier W (2013) Parametric study of vortex structures and their dynamics in swirl-stabilized combustion. Proc Combust Inst 34:3117–3125

Stöhr M, Meier W (2013b) Experimental and numerical study of limit-cycle thermoacoustic oscillations in a gas turbine model combustor. In: Proceedings of the European Combustion Meeting: P4-27

Stöhr M, Boxx I, Carter CD, Meier W (2012) Experimental study of vortex-flame interaction in a gas turbine model combustor. Combust Flame 159:2636–2649

Stöhr M, Arndt CM, Meier W (2013) Effects of Damköhler number on vortex–flame interaction in a gas turbine model combustor. Proc Combust Inst 34:3107–3115

Stöhr M, Arndt CM, Meier W (2015) Transient effects of fuel–air mixing in a partially-premixed turbulent swirl flame. Proc Combust Inst 35:3327–3335

Stopper U, Meier W, Sadanandan R, Stöhr M, Aigner M, Bulat G (2013) Experimental study of industrial gas turbine flames including quantification of pressure influence on flow field, fuel/air premixing and flame shape. Combust Flame 160:2103–2118

Sweeney MS, Hochgreb S, Dunn MJ, Barlow RS (2012) The structure of turbulent stratified and premixed methane/air flames II: Swirling flows. Combust Flame 159:2912–2929

Syred N, Beér JM (1974) Combustion in swirling flows: a review. Combust Flame 23:143–201

Terhaar S, Oberleithner K, Paschereit CO (2015) Key parameters governing the precessing vortex core in reacting flows: an experimental and analytical study. Proc Combust Inst 35:3347–3354

Wehr L, Meier W, Kutne P, Hassa C (2007) Single-pulse 1D laser Raman scattering applied in a gas turbine model combustor at elevated pressure. Proc Combust Inst 31:3099–3106

Weigand P, Meier W, Duan XR, Stricker W, Aigner M (2006) Investigations of swirl flames in a gas turbine model combustor I. Flow field, structures, temperature, and species distributions. Combust Flame 144:205–224

Widenhorn A, Noll B, Aigner M (2009) Numerical study of a non-reacting turbulent flow in a gas turbine model combustor. In: Proceedings of the 47th AIAA Aerospace Sciences Meeting: AIAA 2009-647

TNF Workshop (2015) International Workshop on Measurement and Computation of Turbulent Flames, http://www.ca.sandia.gov/TNF/abstract.html

Worth NA, Dawson JR (2012) Cinematographic OH-PLIF measurements of two interacting turbulent premixed flames with and without acoustic forcing. Combust Flame 159:1109–1126